Biophysical Journal
Article

Biophysical Society

Active Mechanics Reveal Molecular-Scale Force Kinetics in Living Oocytes

Wylie W. Ahmed,[1,2,3,*] Étienne Fodor,[4,5] Maria Almonacid,[6] Matthias Bussonnier,[2,3] Marie-Hélène Verlhac,[6] Nir Gov,[7] Paolo Visco,[5] Frédéric van Wijland,[5] and Timo Betz[2,3,8]

[1]Department of Physics, California State University, Fullerton, California; [2]Laboratoire Physico-Chimie Curie, Institut Curie, PSL Research University, Paris, France; [3]Sorbonne Universités, UPMC Université Paris 06, Paris, France; [4]DAMTP, Centre for Mathematical Sciences, University of Cambridge, Cambridge, United Kingdom; [5]Laboratoire Matière et Systèmes Complexes, Université Paris Diderot, Paris, France; [6]CIRB, Collège de France, and CNRS-UMR7241 and INSERM-U1050, Équipe Labellisée Fondation pour la Recherche Médicale, Paris, France; [7]Department of Chemical Physics, Weizmann Institute of Science, Rehovot, Israel; and [8]Institute of Cell Biology, Center for Molecular Biology of Inflammation, Cells-in-Motion Cluster of Excellence, Münster University, Münster, Germany

ABSTRACT Active diffusion of intracellular components is emerging as an important process in cell biology. This process is mediated by complex assemblies of molecular motors and cytoskeletal filaments that drive force generation in the cytoplasm and facilitate enhanced motion. The kinetics of molecular motors have been precisely characterized in vitro by single molecule approaches, but their in vivo behavior remains elusive. Here, we study the active diffusion of vesicles in mouse oocytes, where this process plays a key role in nuclear positioning during development, and combine an experimental and theoretical framework to extract molecular-scale force kinetics (force, power stroke, and velocity) of the in vivo active process. Assuming a single dominant process, we find that the nonequilibrium activity induces rapid kicks of duration $\tau \sim 300$ μs resulting in an average force of $F \sim 0.4$ pN on vesicles in in vivo oocytes, remarkably similar to the kinetics of in vitro myosin-V. Our results reveal that measuring in vivo active fluctuations allows extraction of the molecular-scale activity in agreement with single-molecule studies and demonstrates a mesoscopic framework to access force kinetics.

INTRODUCTION

Living cells utilize motor proteins to actively generate force at the molecular scale to drive motion and organization in the crowded intracellular environment (1–4). For example, force generation is critical to facilitate the basic tasks of living cells such as spatial organization, motility, division, and organelle transport. Recently, active diffusion has emerged as an important process in cell biology (5–9). Active diffusion is the random motion of intracellular components that is driven by active metabolically powered forces (and not by thermal fluctuations). An interesting example occurs during early vertebrate development, namely, oocyte meiosis, where active diffusion drives nucleus centering (5).

Oocytes are immature female gametes that are destined to be fertilized and grow into a fully functioning organism. They are large cells (80 μm in diameter) of spherical geometry with a thick actin-rich cortex and a well-separated cytoplasmic skeleton (Fig. 1 *A*). The cytoplasmic skeleton of a mouse oocyte is a composite material that includes actin filaments, microtubules, and intermediate filaments. The actin network is composed of long unbranched filaments polymerized from the surface of vesicles that harbor actin nucleating factors (10). These vesicles act as nodes to create an interconnected actin network that is uniform in density throughout the cytoplasm and unpolarized (11), with microtubules that are organized in small seeds and do not form long filaments during prophase-I (12); and although it is probable that intermediate filaments are present (13), little is known about their structure or function in mouse oocytes.

Correct nuclear positioning during prophase-I requires precise spatial and temporal coordination of the cytoskeleton and molecular motors (11,14). Recent work has shown the importance of mechanical processes in oocyte development (5,11,14). Proper spindle positioning requires the oocyte cortex to soften and exhibit plastic deformation (14), and motion of the cytoplasmic actin network is closely regulated by myosin-V motors (11). Motion of large objects, such as positioning of the spindle (14) or nucleus (5), must be driven by a physical force generated by nonequilibrium

Submitted March 31, 2017, and accepted for publication February 8, 2018.

*Correspondence: wahmed@fullerton.edu

Wylie W. Ahmed, Étienne Fodor, and Maria Almonacid contributed equally to this work.

Editor: Jennifer Ross.

https://doi.org/10.1016/j.bpj.2018.02.009

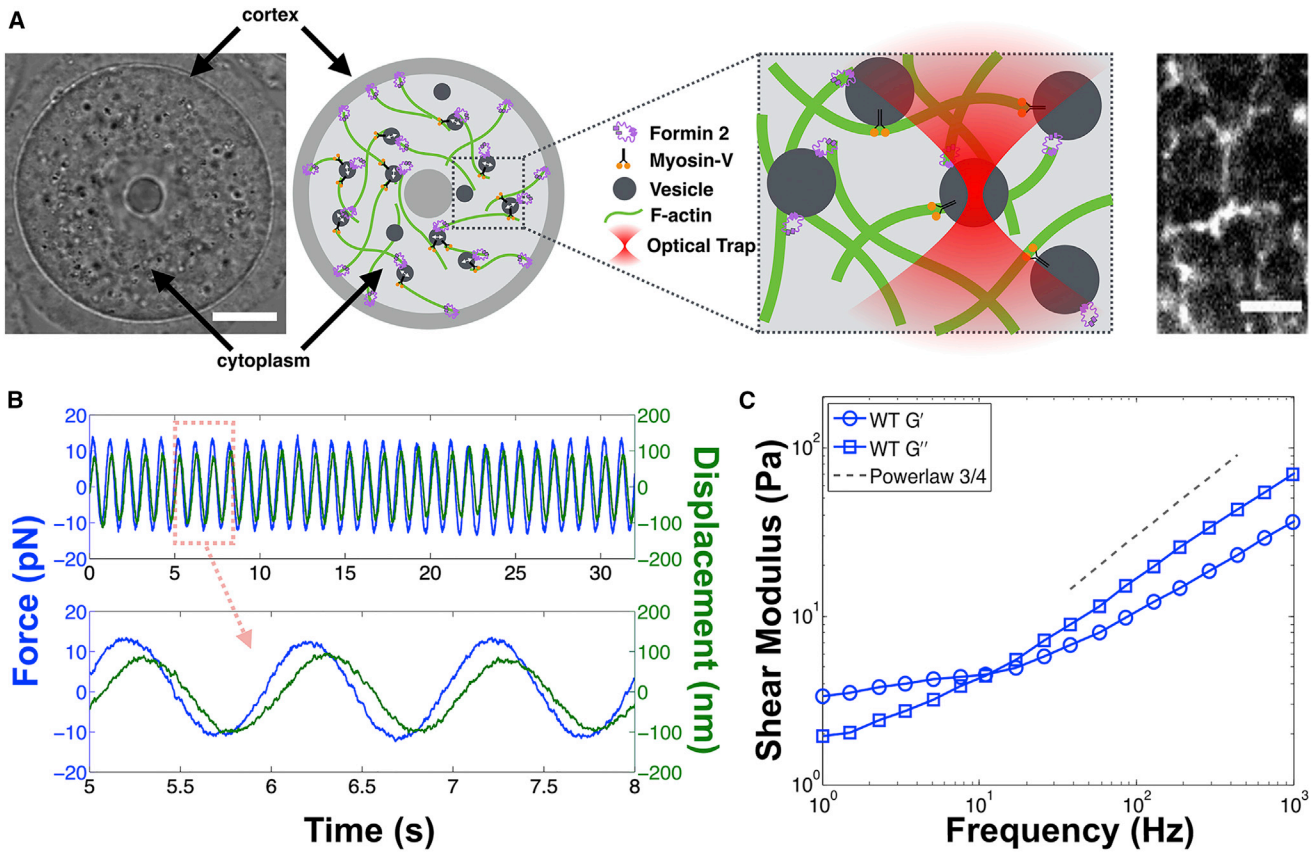

FIGURE 1 Intracellular mechanics surrounding endogenous vesicles in living oocytes. (*A*) Mouse oocytes are large spherical cells that have a well separated cortex and cytoplasmic-skeleton composed of biopolymer filaments (bright-field image, *left*; scale bars, 20 μm). During prophase-I it contains a dynamic actin-myosin-V meshwork that drives vesicle motion (schematic shown in *center* and fluorescent image of actin filaments on *right*; scale bars, 5 μm). Endogenous vesicles embedded in the cytoplasmic-skeleton are trapped using optical tweezers (*zoomed inset*). (*B*) Once a vesicle is trapped, the mechanical properties of the local environment can be measured by AMR where a sinusoidal oscillating force is applied to the vesicle (*blue*) and the resulting displacement of the vesicle is measured (*green*). The viscoelastic shear modulus (G^*) is calculated from this force-displacement measurement via the generalized Stokes-Einstein relation. (*C*) The mechanical properties surrounding vesicles in the cytoplasmic-skeleton of oocytes exhibits power-law behavior with frequency scaling $G^* \propto f^{0.75}$. This shows that the cytoplasmic-skeleton in oocytes can be modeled as a semiflexible polymer network. To see this figure in color, go online.

processes. For instance, we have recently shown that in prophase-I, myosin-V-driven vesicle motion maintains a soft cytoskeleton and generates a force to center the nucleus (5). Here we focus on the physical understanding of the active forces that generate vesicle motion, and how the detailed quantification and modeling of this activity can successfully predict characteristic parameters of the active forces, such as timescales, velocities, and effective forces.

To investigate the nonequilibrium mechanical activity in living cells, it is necessary to independently measure the active force generation and the local mechanical properties to understand how objects move within the complex intracellular environment (15–24). This approach was introduced to study active processes in hair bundles (15) and stress fluctuations in cells (16). Subsequent studies utilized this concept to investigate cross-linked actin-myosin-II networks in reconstituted systems (17), beads embedded in living cells (18–21), and red blood cell membranes (22). Alternative methods of estimating forces in vivo include FRET force sensors, droplet-based sensors, and force inference as recently reviewed (23,24).

In this study, we measure the actively driven motion of endogenous vesicles in the largely unexplored cytoplasmic-skeleton of in vivo mouse oocytes and demonstrate a framework to quantify the underlying driving forces. Endogenous vesicles embedded in the oocyte cytoplasm experience local elastic caging. The vesicles undergo actively driven motion via a sparse actin-myosin-V force-generating network that remodels the environment. The actin-myosin-V network is the key element in generating force for nuclear positioning (5), yet the underlying physical processes related to active force generation are not well understood.

To investigate cytoplasmic force generation, we combine optical tweezer-based active microrheology (AMR) and laser-tracking interferometry with our theoretical framework to quantify the in vivo active mechanical processes and relate them to the underlying stochastic force kinetics (amplitude and temporal correlations). To study the activity

in mouse oocytes, we examine the cytoplasmic-skeleton during prophase-I, when the actin-myosin-V network is the dominant source of activity (5). By using statistical mesoscopic measurements on endogenous vesicles, and theoretical modeling, we extract the molecular-scale force kinetics (average power-stroke duration, displacement, force, and velocity) of in vivo myosin-V.

MATERIALS AND METHODS

Fmn2−/− and myosin-V dominant negative mouse oocytes

To study the effect of the actin-myosin-V network, we utilize two conditions to independently perturb the actin cytoskeleton (Fmn2−/−) and the myosin-V activity (MyoV (−)). Fmn2−/− mouse oocytes have no detectable cytoplasmic actin filaments, as confirmed by several independent studies (14,25–27). The reduced cytoplasmic actin has also been confirmed via cytochalasin-D-treated mouse oocytes, which exhibit the same phenotype and mechanical properties as Fmn2−/− (28) (Fig. S1). For myosin-V dominant negative experiments (MyoV (−)), oocytes were injected with cRNAs using a Femtojet microinjector (Eppendorf, Hamburg, Germany) as published previously (5). Oocytes were kept in prophase-I arrest for 1–3 h to allow expression of fusion proteins. The myosin-Vb dominant negative construct corresponds to a portion of the coiled-coil region of the myosin-Vb that mediates dimerization of the motor (10). We believe this construct binds to the coiled-coil region of endogenous myosin-Vb, resulting in impaired motor dimerization. Thus, myosin-Vb is still able to bind to vesicles and actin filaments but does not actively generate force. It is specific to myosin-Vb and has been shown to stop vesicle motion in mouse oocytes as efficiently as brefeldin A, which is a general traffic inhibitor (5). (Note that MyoV (−) oocytes were referred to as "WT + MyoVb tail oocytes" in a previous study (5).)

Oocyte preparation

Oocytes were collected from 11-week-old mice OF1, 13-week-old C57BL6 (wild-type), or 15-week-old Fmn2−/− female mice as previously described (29) and maintained in prophase-I arrest in M2+BSA medium supplemented with 1 μM Milrinone (30). Live oocytes were embedded in a collagen gel to stop movement of the overall cell during measurements. Collagen gel was made by mixing M2 medium (33.5 μL), 5× PBS (10 μL), NaOH (1 M, 0.9 μL), and collagen (3.6 mg/mL, 55.6 μL) to obtain 100 μL of the final collagen solution at 2 mg/mL with a pH $\sim$ 7.4. Twenty microliters of the collagen solution were deposited on a coverslip and live oocytes were added. The droplet was covered with another glass coverslip using vacuum grease (Dow Corning, Midland, MI) to minimize evaporation. The collagen gel containing oocytes was polymerized in a humid environment at 37°C for 30 min.

Optical tweezer setup

The optical tweezer system utilizes a near-infrared fiber laser (λ = 1064 nm, YLM-1-1064-LP; IPG Photonics, Oxford, MA) that passes through a pair of acoustooptical modulators (AA-Optoelectronics, Orsay, France) to control the intensity and deflection of the trapping beam. The laser is coupled into the beam path via dichroic mirrors (ThorLabs, Newton, NJ) and focused into the object plane by a water immersion objective (60×, 1.2 NA; Olympus, Tokyo, Japan). The condenser is replaced by a long-distance water immersion objective (40×, 0.9 NA; Olympus) to collect the light and imaged by a 1:4 telescope on a InGaAs quadrant photodiode (G6849 QPD; Hamamatsu, Hamamatsu City, Japan). The resulting signal is amplified by a custom-built amplifier system (Oeffner Electronics, Heidelberg, Germany) and digitized at a 500-kHz sampling rate, 16 bits, using an analog input card (PCIe-6353; National Instruments, Austin, TX). All control of the experimental hardware is executed using the software LabVIEW (National Instruments). Optical trapping of endogenous vesicles was calibrated similarly as in (31,32), where the high-frequency fluctuations ($f > 500$ Hz) from the fluctuation and response measurements are aligned to determine the trap stiffness (18,33). This approach assumes that the high-frequency motion is dominated by thermal fluctuations so that the fluctuation dissipation theorem (FDT) holds in this regime. For direct measurement of violation of the FDT, laser tracking interferometry is used first to measure the spontaneous fluctuations of the vesicle, followed immediately by active microrheology to measure the mechanical properties of the local environment surrounding the vesicle.

Laser tracking interferometry

The position of the endogenous particle is measured by back-focal-plane interferometry (34). It should be noted that deformable objects (e.g., giant unilamellar vesicles 10–100 μm) undergo shape fluctuations that will manifest in the voltage measured by the QPD (35). For small endogenous particles ($\sim$1 μm), it has been confirmed that shape fluctuations are small and laser interferometry can be used to track their position with nanometer precision. This has been verified in mammalian cells (36) and yeast (37). A recent study has also confirmed that laser tracking interferometry and the active-power spectrum calibration (31) allow quantitative force-displacement measurements on vesicles in vivo (38). To confirm the validity of this assumption in mouse oocytes, we investigated the deformability of endogenous vesicles and conclude that the majority of measured fluctuations come from active vesicle displacements (see Figs. S4–S9). Additionally, because the endogenous vesicles serve as nodes integrated in the cytoplasmic meshwork, they are accurate reporters of the network mechanics and fluctuations (39).

Data analysis

In the AMR experiments, we apply a known force, F_{ext}, to an endogenous vesicle and measure the resulting displacement, u. Using linear response theory, these are related to the material response function $\chi(t)$ as $u(t) = \int_{-\infty}^{t} \chi(t - t')F_{\text{ext}}(t')dt'$. In Fourier space, we can directly calculate the response function as $\tilde{\chi}(\omega) = \tilde{u}(\omega)/\tilde{F}_{\text{ext}}(\omega)$. To translate the response function into a complex shear modulus G^*, we use the generalized Stokes-Einstein relation $G^* = 1/[6\pi R\tilde{\chi}(\omega)]$, where R is the average radius of the spherical tracers. It can be split into a real part G' and an imaginary part G'', which, respectively, provide information about the elasticlike and viscouslike properties of the medium. For AMR measurements, the laser power exiting the objective was $\sim$120 mW. For the spontaneous fluctuations, we measure the motion, $u(t)$, of endogenous vesicles via laser interferometry (without trapping the vesicle, laser power $\sim$1 mW) and calculate the power spectral density (PSD), $\tilde{C}(\omega) = \int\langle u(t)u(0)\rangle\exp(i\omega t)dt$, as described previously (35). Briefly, we calculate the PSD by using the software MATLAB (The MathWorks, Natick, MA) to take the fast Fourier transform (FFT) of the vesicle position, $\tilde{u} = \text{FFT}(u)$. Then the PSD is calculated as $\text{PSD} = (\tilde{u} \times \tilde{u}^*/p \times s)$, where the asterisk denotes complex conjugate, p is the number of measurement points, and s is the sampling frequency. In systems at thermal equilibrium, the response function can be calculated from the PSD via the FDT as is done for passive microrheology (PMR) (40). Due to the particle size and range of the QPD measurement, our PMR measurements are restricted to a particle displacement of $\sim$500 nm during the measurement interval. If the particle left this regime, that part of the data was not analyzed. The limitation to the linear regime of the detector does not imply that we measure only the linear regime of the

force displacement relation. AMR and PMR data analysis is carried out as done previously (22).

RESULTS

Intracellular mechanics of the oocyte cytoplasmic-skeleton

To measure the local mechanical properties, we optically trap an endogenous vesicle embedded in the cytoplasmic-skeleton, apply an oscillatory force while measuring its displacement (Fig. 1 *B*), and calculate the shear modulus via the generalized Stokes-Einstein relation (41). Because vesicles serve as integrated nodes in the cytoplasmic skeleton, they accurately reflect the mechanics and fluctuations of the network (39) (details on vesicle tracking in the Supporting Material). To calibrate the force on the vesicles, we exploit the established observation that high-frequency fluctuations are thermal in origin (18,31,33). AMR directly measures the mechanical response function ($\tilde{\chi}$), which allows us to determine the complex modulus (G^*) characterizing the viscous and elastic resistance of the composite cytoplasmic skeleton including any contribution from actin, intermediate filaments, microtubules, and other structures present. We find that the cytoplasmic skeleton of oocytes has strongly viscoelastic properties similar to semiflexible biopolymer networks (42,43), exhibiting high-frequency power-law behavior ($G^* \propto f^{\alpha}$, where $\alpha \sim 0.75$) (Fig. 1 *C*). Thus, the cytoplasmic-skeleton in oocytes is strongly frequency-dependent, which must be accounted for when modeling its mechanical behavior. Extending the theoretical model into the viscoelastic regime with a strong frequency dependence is a necessary advancement to describe the intracellular mechanics.

To dissect the mechanical contributions of cytoskeletal filaments in oocytes, we first perform AMR on formin-2 knockout oocytes (Fmn2−/−), which removes cytoplasmic actin filaments nucleated by formin-2 (25), as confirmed via cytochalasin-D experiments as an alternative method of removing actin (Fig. S1). We find that the mechanical properties do not change compared to WT, indicating that the actin network does not provide significant mechanical resistance in the oocyte (Fig. 2, *A* and *B*). This behavior is presumably because the actin network in WT oocytes is sparse (Fig. 1 *A*, *right* and Fig. S2), with a mesh size of 5.7 ± 1.9 μm (26). Depolymerizing the microtubules by nocodazole treatment (1 μM) does not significantly affect the mechanical properties (Fig. 2, *A* and *B*), indicating that microtubules also do not provide significant mechanical resistance in the cytoplasmic-skeleton. This result is expected because prophase-I microtubules form small seeds instead of long force-bearing tubule structures (12). These combined results suggest that there are other mechanical scaffolds contributing to the stiffness in the cytoplasm of mouse oocytes.

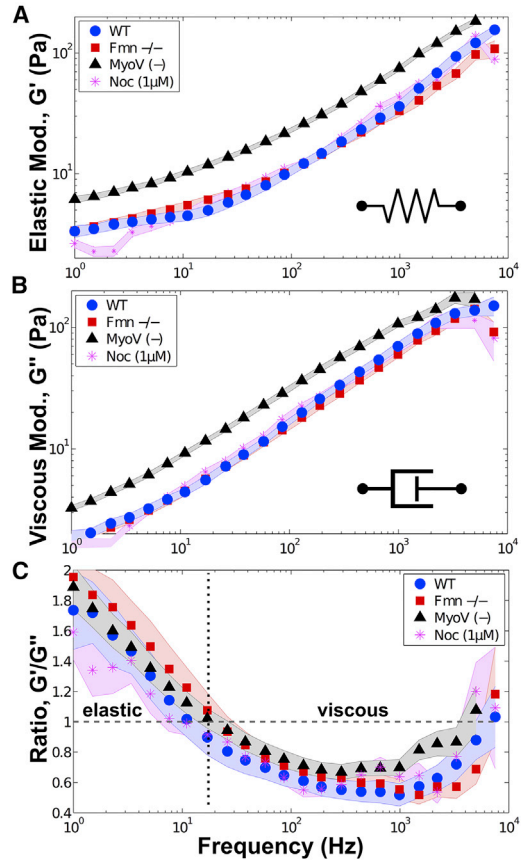

FIGURE 2 The cytoplasmic-skeleton of mouse oocytes is viscoelastic. (*A* and *B*) Insets indicate that G' quantifies the elasticity and G'' quantifies the viscous dissipation of the cytoplasmic-skeleton. The local mechanical properties (elastic and viscous) surrounding vesicles does not change from WT (*blue*, ○) when actin (*red*, □) or microtubules (*magenta*, *) are absent. However, when myosin-V is inactivated (*gray*, △), the cytoplasmic-skeleton stiffens significantly (Kolmogorov-Smirnov test, $p < 1 \times 10^{-7}$), showing that the absence of an active actin-myosin-V meshwork leads to a stiffer mechanical environment surrounding vesicles in oocytes. (*C*) The ratio of the elastic and viscous moduli (G'/G'' in all oocytes shows that the cytoplasmic-skeleton is more elastic at lower frequencies and more viscous at higher frequencies with a crossover at ∼10–20 Hz. This shows the highly viscoelastic nature of the oocyte cytoplasmic-skeleton. (sample size = WT: 11 cells, 32 vesicles; Fmn2−/−: 10 cells, 33 vesicles; MyoV (−): 23 cells, 69 vesicles; Noc (1 μM): 8 cells, 52 vesicles; shaded region indicates mean ± SE. (Note: data at 10 Hz in *A* and *B* are presented in a different context in (5).) To see this figure in color, go online.

Although our results show that actin does not contribute significantly to the mechanical resistance, it is known that the actin-myosin-V meshwork activity plays a critical role for self-organization, such as positioning of the meiotic spindle (25,26) and nucleus centering in mouse oocytes (5). To independently probe the activity of this network, we impaired the myosin-V motor force generation by deactivating it via microinjection of a dominant negative construct (MyoV (−)) (5,10) (see Materials and Methods). Under these conditions, the mechanical properties of the cytoplasmic-skeleton stiffens significantly as evidenced by

the shift upwards in the elastic and viscous moduli (Fig. 2, *A* and *B*). This increased mechanical stiffness correlates with a higher density actin meshwork that is observed in the absence of myosin-V activity (Fig. S2), and can be explained by increased cross-linking (11). Actin networks are known to stiffen significantly upon addition of cross-links, as long as the inter-cross-link distance is smaller than the persistence length.

The overall behavior of the cytoplasmic skeleton in oocytes is strongly viscoelastic, where neither the elastic or viscous components dominate by a large margin. At the lowest probed frequencies, the behavior is slightly more elastic, with a crossover (~10–20 Hz) to more viscous at higher frequencies. However, both components of the shear moduli are always within a factor of two at the observed frequencies (Fig. 2 *C*). This is in contrast to adherent cells, which typically show an overall weaker frequency dependence and are dominantly elastic (18,44).

Quantifying in vivo active force fluctuations

To quantify nonequilibrium activity, we use laser-tracking to precisely measure the spontaneous motion of vesicles in the cytoplasmic-skeleton with high spatio-temporal resolution (34,36,37) (see Materials and Methods). Both the spontaneous motion and the local mechanics are measured for each individual vesicle via active microrheology and laser interferometry. This allows direct comparison between the local mechanical environment experienced by the vesicle and the active force that is driving its motion because both measurements are made in situ. This is critical to extract information about the molecular-scale processes. In the absence of biochemical activity, the motion of the vesicles would be due to purely thermal agitation, which is fully determined by the mechanical properties of the system. This basic relation is given by a fundamental theorem of statistical mechanics known as the FDT (40). The FDT relates the small fluctuating motion of the vesicles to the mechanical properties of the surrounding environment by $\tilde{\chi}'' = \pi f \tilde{C}/k_B T$, where $\tilde{\chi}''$ is the dissipative part of the mechanical response, $\tilde{C}$ is the power spectral density of vesicle motion, f is the frequency, k_B is the Boltzmann constant, and T is the temperature (see Table 1 for a list of symbol definitions). However, in living cells, the presence of biochemical activity gives rise to active forces (e.g., a nonequilibrium process) driven by energy consuming processes (15,16,45). In other words, the force driving the motion of particles in a living cell (e.g., the oocyte) has two contributions: 1) a passive (purely thermal) contribution described by classical equilibrium physics; and 2) an active contribution that is biochemically regulated and cannot be understood via equilibrium physics.

We quantify and explain both the passive and active contributions driving intracellular fluctuations, by independently measuring the response function and power spectral density. We use AMR to measure $\tilde{\chi}$ and laser-tracking to measure $\tilde{C}$, and use this information to check for violation of FDT (15,17,46), which indicates active force generation. In oocytes, at high frequencies the mechanical response ($\tilde{\chi}''$) and the spontaneous vesicle motion ($\pi f \tilde{C}/k_B T$) are related by the FDT, as expected for thermal fluctuations (18,33) (Fig. 3 *A*). At frequencies <~400 Hz, the observed motion of vesicles is dominated by an active energy-consuming process (highlighted by the *pink shaded region between the two curves* in Fig. 3 *A*).

To quantify the nonequilibrium activity in an active soft material, it is instructive to consider the effective energy (15,47–49), $E_{\text{eff}} = \pi f \tilde{C}/\tilde{\chi}''$, which is a measure of how far the system is from thermal equilibrium. Note that the measurement of E_{eff} requires two separate measurements: rheology to get $\tilde{\chi}''$ and laser interferometry to get $\tilde{C}$. WT oocytes exhibit a strong departure from equilibrium due mainly to the actin-myosin-V network activity. Accordingly, the deviation is reduced when either actin is absent (Fmn2−/−) or myosin-V is inactivated (MyoV (−)) (Fig. 3 *B*). This is quantitative confirmation that the dynamic actin-myosin-V meshwork drives vesicle dynamics out-of-equilibrium in the cytoplasmic-skeleton of mouse oocytes (5,11). Note that in Fmn2−/− and MyoV (−) not all activity is abolished, which is presumably due to residual

TABLE 1 List of Symbols, Variables, and Definitions

$\tilde{\chi}$ (ω) (m/N)	response function	T (K)	bath temperature
ω (rad/s)	frequency	T_A (K)	active temperature
$\gamma(t)$ (N/m)	memory kernel	τ (s)	active persistence time
$G^*(\omega)$ (N/m^2)	complex shear modulus	τ_0 (s)	active waiting time
$G'(\omega)$ (N/m^2)	elastic modulus	v (m/s)	active burst amplitude
$G''(\omega)$ (N/m^2)	viscous modulus	$\tilde{C}$ (ω) (m^2-s)	position power spectral density
R (m)	vesicle radius	$E_{\text{eff}}(\omega)$ (N-m)	effective energy
κ (N/m)	local cage stiffness	$\tilde{F}_{\text{cell}}$ (ω) (N-s)	total cell force
ζ_α (s)	passive timescale	$S_{\text{cell}}(\omega)$ (N^2-s)	cell force spectrum
α	power-law exponent	$S_{\text{thermal}}(\omega)$ (N^2-s)	thermal force spectrum
$x(t)$ (m)	vesicle position	$S_{\text{active}}(\omega)$ (N^2-s)	active force spectrum
$x_0(t)$ (m)	local cage position	F (N)	active force amplitude
$\xi(t)$ (N)	thermal noise	v_{vesicle} (m/s)	average vesicle velocity
$v_A(t)$ (m/s)	active burst noise	Δx (m)	average step-displacement

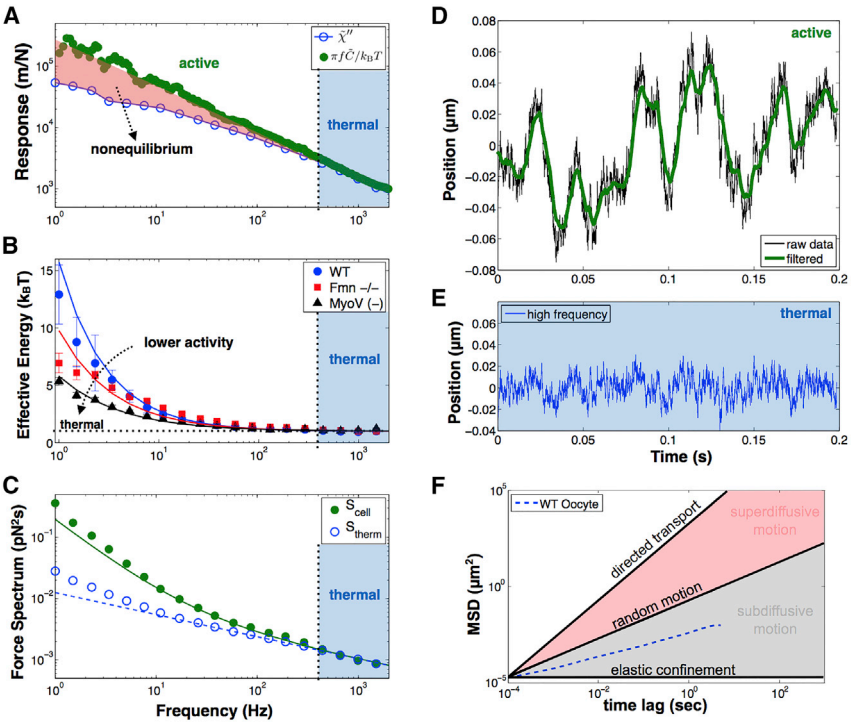

FIGURE 3 Active force generation by myosin-V drives the cytoplasmic-skeleton out-of-equilibrium. (*A*) At frequencies below 400 Hz the spontaneous motion of vesicles in WT oocytes (*green circles*) is larger than expected for thermal equilibrium (*blue circles*). This shows that active forces are contributing to vesicle motion in this regime as highlighted by the red shaded region. This is direct evidence of nonequilibrium behavior in the cytoplasmic-skeleton (via violation of the FDT). At high frequencies the observed vesicle motion resembles thermal motion indicated by the blue-shaded region. (*B*) WT oocytes (*blue*) are the furthest from equilibrium as shown by their higher effective energy. In the absence of actin (*red*) or when myosin-V is inactivated (*black*) the dynamic actin-myosin-V meshwork is compromised, and oocytes have lower effective energy. Solid lines are theoretical fits (see equations in the Supporting Material; error bars = mean ± SE). (*C*) The cell force spectrum (S_{cell}) experienced by vesicles is the sum of thermal forces (S_{therm}) and active forces (S_{active}). At high frequencies S_{cell} (*green*) is dominated by S_{therm} (*blue*) and the two spectra coincide (*blue shaded region*). At lower frequencies S_{cell} is larger than S_{therm} showing the existence of additional active forces. Solid and dashed lines are theoretical predictions (see equations in the Supporting Material), low-frequency deviation is due to simple power-law model. Standard error of experimental data is within marker size. (*D*) When a representative trajectory (*black*) is filtered to remove the high-frequency thermal fluctuations the result is a smoothed trajectory (*green*) that represents actively driven motion. The difference between the true trajectory (*gray*) and the smoothed trajectory (*green*) recovers the high-frequency thermal fluctuations (*blue*) shown in (*E*). (*F*) The MSD of vesicles, calculated from trajectory data, indicates they undergo random-confined motion in the oocyte cytoplasmic-skeleton at short timescales. This behavior transitions to active diffusion at longer times (5), and is reminiscent of cytoplasmic stirring (33). To see this figure in color, go online.

actin-myosin-V that is active or other remaining sources of nonthermal activity in the oocyte (e.g., enzymes, polymerization, myosin-II in the cortex (11).

To develop a more intuitive picture of the activity, we quantify the forces generated in the cell by calculating the cell force spectrum (S_{cell}). The S_{cell} directly represents the average total force on a vesicle from all stochastic sources (active and thermal) inside the cell, and has been used by several previous studies to quantify activity (16,18,19,46). The force spectrum is a convenient and common way to quantify the total intracellular forces. In analogy to the force on a simple spring, where the force is the stiffness multiplied by displacement ($F = \kappa\Delta x$, where κ is stiffness and Δx is displacement), we calculate $S_{cell} = (6\pi R)^2|G^*|^2\tilde{C}$, where $|G^*|^2$ represents the stiffness of the cytoplasmic-skeleton (18,19,50). In our framework we separate the total force spectrum in the cell to be the sum of thermal forces and active forces ($S_{cell} = S_{therm} + S_{active}$) (46,51). The thermal force spectrum is calculated directly from the AMR measurements as $S_{therm} = 12\pi RG''k_BT/\omega$, where R is the vesicle radius, G'' is the dissipative component of the shear modulus, and $\omega = 2\pi f$ is frequency. S_{therm} represents the forces present at thermal equilibrium and is a direct consequence of the FDT (40). The resulting force spectrum is shown in Fig. 3 *C*, where at high frequencies the cell force spectrum (S_{cell}) is dominated by thermal forces (where $S_{active} << S_{thermal}$) as expected, but at lower frequencies ($f < 400$ Hz) active forces dominate ($S_{active} >> S_{thermal}$), which results in higher total force experienced by vesicles in the cytoplasm over thermal equilibrium (*lines* represent the theoretical model (52) introduced in the next section). To visualize the effect of thermal and active forces, we show a representative trajectory of a vesicle (Fig. 3 *D*, *black*). Based on our measured violation of FDT (Fig. 3 *A*), we apply a filter to isolate the low-frequency (<400 Hz) vesicle motion that is mainly due to active processes (Fig. 3 *D*, *green*), and the high-frequency motion that is dominated by thermal fluctuations (Fig. 3 *E*).

Modeling actively driven vesicle motion

Mouse oocytes in prophase-I exhibit nondirected motion of vesicles in a viscoelastic environment (Fig. 3 *F*, *blue*) due to a unique cytoplasmic network (Fig. 4 *A*). We use this picture to motivate our theoretical model of generic active forces in the cell cytoplasm and do not impose any physical assumptions on the origin of that force. Therefore, our model lumps all active forces together as a single dominant process, regardless of their origin. To gain access to the molecular-scale kinetics of the dominant active process driving the

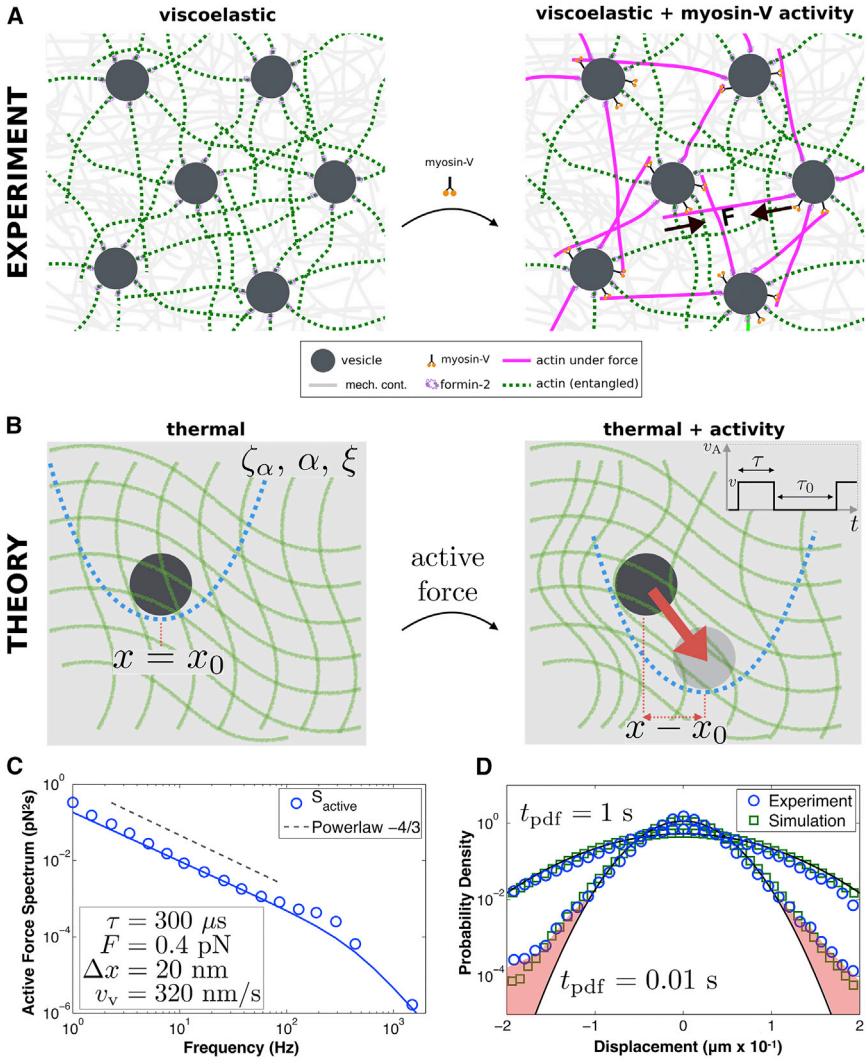

FIGURE 4 A theoretical model of active mechanics connects in vivo measurements to molecular force kinetics. (*A*) Vesicles (*dark gray*) are embedded in the complex mechanical continuum (*gray background*) of the oocyte interior. Actin filaments emanate from the surface of vesicles creating an entangled network (*green*, *left*). Myosin-V motors generate force on actin (*magenta*, *right*) giving rise to forces throughout the network driving random motion of vesicles. (*B*) We model vesicles embedded in a mechanical continuum with local cage stiffness (κ) represented by the blue harmonic potential, viscoelastic dissipation (ζ_α,α), and thermal fluctuations (ξ) (*left*). Active processes rearrange the network through bursts of motion (v_A), resulting in displacement of the local cage (*blue harmonic*), which generates the active force ($\kappa\zeta_\alpha v$, *red arrow*) that drives vesicle motion toward the local minimum (*right*) (inset indicates active force kinetics). (*C*) The active force spectrum (S_{active}) quantifies the forces on vesicles due to only active processes. Combined with our quantitative model we find that the vesicles are subject to 0.4 pN of force, during a power stroke of length $\Delta x \sim 20$ nm and duration 300 μs, resulting in a vesicle velocity of 320 nm/s, which is strikingly similar to the kinetics measured for single molecule myosin-V in vitro and the in vivo vesicle velocity. The solid line is the theoretical fit (Eq. 7), and the dotted line is a −4/3 power law consistent with the cytoplasmic-skeleton mechanics. (*D*) Simulated vesicle motion (*green squares*) agrees with experimental data (*blue circles*) for a wide range of timescales as shown by the probability distribution of displacements. This includes long timescale ($t_{pdf} = 1$ s) Gaussian behavior and short timescale ($t_{pdf} = 0.01$ s) non-Gaussian tails (indicated by *red-shaded regions*) that suggest molecular motor behavior, where t_{pdf} is the time-lag for calculation of the displacement correlations. Gaussian distributions shown in black. These results show that molecular level kinetics of active processes can be extracted from mesoscopic in vivo measurements. To see this figure in color, go online.

cytoplasmic interior of oocytes, we developed a quantitative model describing vesicles embedded in a viscoelastic environment that are subjected to thermal and active forces. Here, the nonequilibrium processes provide the active forces that reorganize the polymer cytoskeleton and drive motion of the vesicles. Our theoretical framework extends previous approaches for near-elastic networks (46,50,53) to include the complex mechanical properties measured experimentally (Fig. 2).

We begin by using the traditional Langevin equation to describe a vesicle freely fluctuating in a viscoelastic continuum where the left side of Eq. 1 is the drag force on the vesicle and the right side includes the elastic caging force from the cytoskeleton (with stiffness κ) and the thermal force. It is an application of Newton's second law on the fluctuating vesicle. Equation 1 describes how a vesicle thermally fluctuates randomly about its equilibrium position, but on average will not move from its original position due to elastic caging of the cytoskeleton:

$$\int^{t} \mathrm{d}t'\gamma(t-t')\dot{x}(t') \;=\; -\kappa(x-x_0)+\xi, \qquad (1)$$

where x is the position of the vesicle; x_0 is the position of the elastic cage; ξ is thermal force taking the form of Gaussian colored noise with correlations $\langle\xi(t)\xi(t')\rangle = k_B T\gamma(|t-t'|)$, as provided by the FDT (40); k_B is the Boltzmann constant; and T is the bath temperature of the environment. The viscoelastic material properties are modeled as a soft glassy material, where κ is the harmonic trap stiffness centered at x_0, and the memory kernel is $\gamma(t) = \kappa(\zeta_\alpha/t)^\alpha/\Gamma(1-\alpha)$,

where Γ is the Gamma function, α is the viscoelastic power-law frequency dependence, and ζ_α is a passive timescale of the material (see Table 1 for symbol definitions and the Supporting Material for details). In an attempt to capture the active vesicle dynamics, we introduce Eq. 2, which phenomenologically describes how nonthermal forces remodel the cytoplasmic-skeleton and determine the dynamics of the elastic caging, as

$$\int^{t} \mathrm{d}t' \gamma(t-t')\dot{x}_0(t') = \kappa\zeta_\alpha v_A, \tag{2}$$

where the left side is the drag force on the cage and the right side is the active nonthermal force that drives motion of the cage. Equation 2 is an application of Newton's second law on the elastic cage, which is a geometric constraint, and fundamentally does not have mass. In this case, the cage represents the confining effects of the cytoplasmic skeleton and thus is endowed with the mass of this surrounding material and its center of mass corresponds to the center of the cage. The equilibrium position of the cage is x_0 and the active force is $\kappa\zeta_\alpha v_A$, where v_A is the velocity of the cage motion. For completeness, Eq. 2 should include the force applied on the cage by the vesicle (the action-reaction principle) and the thermal force on the cage itself. However, when each increment of vesicle motion is small compared to the cage size, these forces do not affect the cage dynamics to leading order and previous work has suggested they can be neglected (see Eq. 3, a and b, in (50)). The overall dynamics describe a vesicle in the cytoplasmic-skeleton that experiences an elastic caging (Eq. 1), until active forces act to remodel the cytoskeleton and move the cage (Eq. 2), resulting in a vesicle motion driven by both thermal and active forces. This can be considered a coarse-grained approach, where the dynamics are divided into two equations of motion describing the thermal fluctuations (Eq. 1) and the active motion (Eq. 2) to simplify the mathematics and subsequent analysis. Therefore, this phenomenological model can describe diffusive-like motion driven by nonthermal forces in a viscoelastic medium, also known as "active diffusion." Interestingly, a recent study used a coarse-grained two-fluid continuum model (54) and arrived at the same conclusion (46).

The parameters characterizing the mechanical properties are obtained from AMR measurements. The memory kernel quantifies the mechanical resistance of the cytoplasmic-skeleton and influences the dynamics of both the vesicle, x, and the cage, x_0. In principle, one would expect the memory kernel in Eqs. 1 and 2 to be different because Eq. 1 describes motion of the vesicle, and Eq. 2 describes motion of the cage. Provided that the dissipation is mediated by the surrounding medium in both cases, then the memory kernels would only differ by a prefactor. In this model, the prefactor ends up on both sides of Eq. 2 and mathematically cancel, leaving the memory kernels in Eqs. 1 and 2 identical (see previous derivation (50)).

The microscopic interpretation of κ is the local caging due to the cytoskeleton (as evident from the low-frequency plateau in the measured shear modulus Fig. 2), where x_0 is the location of this cage. In the absence of active forces, the position of this local cage does not move ($\dot{x}_0 = 0$). When active forces do exist, as in living cells, they rearrange the cytoskeleton and drive motion of the cage ($\dot{x}_0 \neq 0$). The active force experienced by the cage results from the active burst velocity, v_A, which is a stochastic process consisting of alternating active and quiescent periods. During an active phase, the active burst velocity, v_A, takes on a constant nonzero value, v, for a random exponentially distributed time of average value τ. During a quiescent phase, the active burst velocity is 0 for an exponentially distributed random time of average value τ_0 (46,48,50). A schematic example is shown in Fig. 4 *B* (*right inset*). The active burst velocity is a zero-mean stochastic process with correlations $\langle v_A(t)v_A(0)\rangle = k_B T_A \exp(-|t|/\tau)/(\kappa\zeta_\alpha\tau)$, where $k_\mathrm{B}T_A = \kappa\zeta_\alpha(v\tau)^2/[3(\tau+\tau_0)]$ defines an active energy scale. Note that the dynamics of the joint process $\{x, x_0\}$ is not Markovian because of the memory kernel in the equations of motion.

From the generalized Stokes-Einstein relation, the memory kernel can be associated with a complex shear modulus $G^* = G' + iG''$ of the form

$$G'(\omega) = \frac{\kappa}{6\pi R}\left[(\omega\zeta_\alpha)^\alpha \cos\left(\frac{\pi\alpha}{2}\right) + 1\right], \tag{3}$$

$$G''(\omega) = \frac{\kappa}{6\pi R}(\omega\zeta_\alpha)^\alpha \sin\left(\frac{\pi\alpha}{2}\right). \tag{4}$$

This model separates the passive forces that originate from the thermal fluctuations of the medium and the active forces that depend on the energy-consuming processes in the active material. Note that if the active force on the cage is zero ($\kappa\zeta_\alpha v_A = 0$), then Eq. 2 is zero, and the equation of motion simplifies to confined viscoelastic Brownian motion (Eq. 1). If the active force is not zero, then it originates from an active process that has steplike velocity kinetics (Fig. 4 *B*, *right inset*). These force kicks drive the nonequilibrium fluctuations in our model.

The nonequilibrium properties of the active force are quantified by the deviation from the FDT defined by a frequency-dependent effective energy, E_eff, as discussed earlier. We compute it in terms of the microscopic ingredients of our theoretical model,

$$E_\mathrm{eff}(\omega) = k_\mathrm{B}T + \frac{1}{(\omega\zeta_\alpha)^{3\alpha-1}\sin(\pi\alpha/2)}\frac{k_\mathrm{B}T_A}{1+(\omega\tau)^2}, \tag{5}$$

where k_BT_A is the energy scale associated with the active process. The dynamics of the tracer can be written as: $x(t) = \int dt' \chi(t - t') F_{cell}(t')$, where $F_{cell} = \xi + \kappa x_0$ is the cell force that describes the thermal forces arising in the cell and the effect of the active forces via x_0. Explicitly, we calculate the cell force spectrum as $S_{cell} = \langle |\tilde{F}_{cell}|^2 \rangle = \langle |\tilde{\xi}|^2 \rangle + \kappa^2 \langle |\tilde{x}_0|^2 \rangle$, which corresponds to the spectrum calculated previously as $S_{cell} = \tilde{C}/|\tilde{\chi}|^2 = (6\pi R)^2 |G^*|^2 \tilde{C}$ from experiments. Because we separate the thermal and active contributions to the force spectrum in our model, we compute the explicit expressions for each as

$$S_{therm}(\omega) = 2k_B T \kappa \zeta_\alpha (\omega \zeta_\alpha)^{\alpha - 1} \sin\left(\frac{\pi\alpha}{2}\right), \quad (6)$$

$$S_{active}(\omega) = \frac{2\kappa\zeta_\alpha}{(\omega\zeta_\alpha)^{2\alpha}} \frac{k_B T_A}{1 + (\omega\tau)^2}. \quad (7)$$

The active force spectrum (Eq. 7) can now be used to extract the kinetics of the active force. Details of the derivation can be found in the Supporting Material.

Extracting in vivo molecular-scale force kinetics

By combining our analytical model and experimental measurements, we extract the force kinetics driving active mechanical processes in the oocyte. First, the mechanical measurements from AMR were fit to Eqs. 3 and 4 to determine the mechanical parameters: α, ζ_α, and κ from the data shown in Fig. 2, *A* and *B*. Once the mechanics is determined, the remaining equations are largely constrained. The best fit of the data for effective energy (Fig. 3 *B*) is used to determine k_BT_A in Eq. 5, where the fit is independent of τ when $\tau < 10$ ms. From fitting the active force spectrum, we find that $\tau = 0.3$ ms (the only free parameter) to capture the high-frequency dropoff (Fig. 4 *C*). The fit parameters for the theoretical model applied to all experimental conditions are shown in Table 2. To summarize: α, ζ_α, and κ are obtained from fitting AMR measurements of the mechanics (G',G''), T_A/T is obtained from fitting the effective energy data (E_{eff}), and τ is obtained from fitting the active force spectrum (S_{active}). Our model extracts the molecular-scale force kinetics directly from fitting the active force spectrum.

TABLE 2 Theoretical Fit Parameters

	Mechanical Properties			Activity	
	α	ζ_α (s)	κ (pN • μm^{-1})	T_A/T	τ (ms)
Wild-type	0.64	0.0657	20	5.5	0.30
Fmn2−/−	0.6	0.103	18	5.0	0.15
MyoV (−)	0.57	0.163	27	3.8	0.1
	from AMR			from AMR/PMR	

As a result, we are able to capture the short-timescale power stroke (τ) of the active process, which is not possible from fitting the long-timescale plateau of the mean squared displacement (MSD) as done previously (18,33).

To investigate how well our estimated kinetic parameters describe our experimental data, we turn to Brownian dynamics simulations. We use the measured parameters (mechanics, kinetics, etc.) extracted from the AMR measurements and force spectrum to simulate vesicle dynamics via a stochastic equation of motion (see the Supporting Material) using previously developed methods (55,56). These simulations of vesicle motion use, exclusively, values measured from experiment, without any free parameters. At this point, it is important to note that the fit parameters in Table 2 are based on first and second moment analysis from experimental data, and they do not capture a priori the full distribution of vesicle dynamics, especially the non-Gaussian behavior that depends on the details of higher-order moments of the active burst statistics.

To test this, we analyze the simulations by calculating the full probability distribution of the simulated vesicle displacements (also known as "van Hove correlations" (57)) and compare them to our experimental measurements (Fig. 4 *D*). We find that the statistics of the simulated vesicle motion is in excellent agreement with the measured spontaneous motion of vesicles in living oocytes. Measured and simulated motion of vesicles is nearly identical, including the central Gaussian region and the non-Gaussian tails (*shaded red* in Fig. 4 *D*) at short timescales. This non-Gaussian behavior suggests molecular motor activity that is dominated by the single most persistent motor closest to the vesicle (58). Whereas our analytic model describes the mean values of the experimental measurements, these simulations exploit the full range of data by capturing the entire distribution of displacement correlations from experiments. In other words, there was no guarantee simulations would agree with the experiments, particularly for the tails of the distribution (or any other non-Gaussian behavior). Hence, the agreement found between simulations and experiment is nontrivial and supports the estimated kinetic parameters and use of the memory kernel acting on both the vesicle and the cage. These results show that our model of steplike active forces captures the overall motion of vesicles (including higher-order statistics) in the cytoplasmic-skeleton of living oocytes.

DISCUSSION

Myosin-V activity maintains a soft cytoplasmic-skeleton

Our mechanical measurements (AMR) indicate that when myosin-V activity is present, the cytoplasmic-skeleton in oocytes is softer. This observation was first reported by Almonacid et al. (5), and the new data in this study extends this

observation across a wide range of frequencies. Additionally, the combined measurements of viscoelastic properties and spontaneous vesicle motion provides access to an independent measurement of mechanics and activity. The mechanism of how softening occurs is not yet clear, but may be related to the structural connectivity of the actin-myosin-V network. In our experiments, it is possible that when myosin-V is inactivated (MyoV (−)), it serves as a passive cross-linker that stiffens the environment or cross-links the vesicle to the network. Because cross-linking leads to highly nonlinear stiffening (59) (if cross-link distance is not large compared to the persistence length), a small change in cross-linking could effectively increase the stiffness of the cytoplasmic-skeleton. Alternatively, the presence of myosin motors may reduce the mechanical contribution of the actin cytoskeleton by causing fluidization (see (60)) so that other intracellular structures (e.g., intermediate filaments) dominate the mechanics in the WT condition. This interpretation is also consistent with the finding that the removal of the cytoplasmic actin has no effect on the shear modulus. However, in the absence of experimental tools to dissect the mechanical contribution of all cytoplasmic components in the mouse oocyte, the answer to this question is currently out of reach.

Active force spectrum reveals molecular-scale kinetics of the active process

Myosin-V is typically considered a directed transport motor. However, in prophase-I mouse oocytes, myosin-V drives vesicle motion in a nondirected fashion as evidenced by its sublinear scaling of the MSD (Fig. 3 *F*, *blue*). Previous work has also shown that myosin-V drives random motion of vesicles (active diffusion) on longer timescales of minutes (5). To further illustrate this point, Fig. 4 *A* (*left*) shows a schematic illustration of vesicles and actin filaments embedded in the oocyte interior. The complex mechanical environment is represented by a generic continuum (*gray background*). When myosin-V is attached to a vesicle and applies force on an actin filament, this force is transduced through the actin filament to a neighboring vesicle where it is bound by formin-2 (e.g., *black arrows* in Fig. 4 *A*, *right*). This process occurs frequently throughout the oocyte interior, resulting in randomly distributed force-dipoles (similar to myosin-II in some systems (17,33)). Thus, each vesicle experiences forces in random directions due to the action of myosin-V throughout the network. This is represented by many actin filaments under force, as shown in magenta in Fig. 4 *A* (*right*). Therefore, due to the unique network connectivity in the cytoplasmic-skeleton, myosin-V motors drive active random motion in prophase-I mouse oocytes reminiscent of cytoplasmic stirring observed previously that was driven by myosin-II (33). This actin-myosin-V activity is expected to be the dominant driver of active diffusion in our system (5).

By looking at the active force spectrum in WT oocytes, we can characterize the kinetics of the dominant active process. The first factor in Eq. 7 depends on the mechanical properties of the cytoplasmic-skeleton whereas the second factor is related to the kinetic properties of the active processes. This illustrates that the active force spectrum is dependent on the active force generation as well as the mechanics of the environment it must push against. The power-law scaling of the active force spectrum contains information about the underlying physics. At lower frequencies the active force spectrum scales as $f^{-2\alpha}$, reflecting the active forces pushing against the viscoelastic environment. At higher frequencies the active force spectrum is dominated by the kinetics of the active force generation process, which scales as $f^{(-2\alpha+2)}$. This is illustrated in Fig. S3, where at low frequencies there is a power-law dependence of $-4/3$ consistent with the mechanics ($\alpha \approx 2/3$) and at high frequencies the power-law dependence is $\sim -10/3$ consistent with kinetics and mechanics. The crossover between these two regimes occurs at $1/\tau$ as shown approximately by the purple dotted line (Fig. S3).

Our predicted active force spectrum exhibits power-law scaling that is dependent on the mechanical properties of the system (α), in contrast to previous studies (16,53,61). Previous theoretical developments predict an active force spectrum that scales as f^{-2}, which is independent of the mechanical properties (16), and a plateau (f_0) below a critical frequency (Eq. 2 in (33) and Eq. S1 in (18)). It is worth noting that in the near-elastic case ($\alpha \sim 0$), our model recovers the behavior observed in previous work (18,33). The divergence of the active force spectrum at low frequencies is consistent with our experimental measurements, and others, where a low-frequency plateau is not observed (18,19,21,62).

The experimental measurements for the active force spectrum ($S_{\text{active}} = S_{\text{cell}} - S_{\text{therm}}$) and theoretical model are compared in Fig. 4 *C*. The low-frequency power-law behavior is clearly seen, whereas at higher frequencies the active forces drop off rapidly, which may reflect molecular motor statistics (63). This allows us to calculate other kinetic parameters, such as the apparent active force amplitude, *F*, which is the typical force amplitude that an endogenous vesicle feels that drives its nonthermal motion:

$$F = [3\kappa k_B T_A(\tau + \tau_0)/\zeta_\alpha]^{1/2}, \tag{8}$$

where τ_0 is deduced from the single-molecule myosin-V duty cycle (64) (see details in the Supporting Material). Here, *F*, lumps all activity into one value to quantify the active force. Once this force is known it is also straightforward to calculate the typical vesicle velocity,

$$v_{\text{vesicle}} = \frac{F}{\kappa\zeta_\alpha}, \tag{9}$$

which is a ratio of the driving force, and the resistance provided by the surrounding environment, $\kappa\zeta_\alpha$. Using this argument, the typical vesicle displacement induced by one force kick can be computed as $\Delta x = F/\kappa$. Thus, once the timescale of the force kick (τ) is extracted from Eq. 7, the apparent force felt by the vesicle (F), the expected vesicle velocity (v_v), and the step-size Δx can be deduced.

Our combined experimental and theoretical framework allows access to the molecular-scale kinetics via mesoscopic measurements of the active force spectrum (Fig. 4 *C*). The active force spectrum, S_{active}, has only one free fitting parameter, τ, which corresponds to the molecular-scale activity. All other model parameters are fixed previously. In living oocytes we find that endogenous vesicles experience a force of $F \sim 0.4$ pN during a power stroke of $\tau \sim 300$ μs duration, with a step-size of $\Delta x \sim 20$ nm. This is strikingly similar to single molecule myosin-V kinetics measured in vitro (see Table 3) (63–69). In addition, we find that the predicted average vesicle velocity due to active forces is $v_{\text{vesicle}} \sim 320$ nm/s, which is in agreement with myosin-V velocity in vitro (65–67), as well as the velocity of myosin-V driven vesicles measured in in vivo oocytes via video microscopy (5,10). Whereas our model does not assume the action of a single motor acting on the vesicle, the extracted kinetics are in agreement with single myosin-V. Because it is likely there are several motors affecting the vesicle dynamics, our results suggest that the myosin-V motors in prophase-I oocytes do not act simultaneously, thus allowing individual motor kicks to be observed. Interestingly, previous work has estimated the number of motors involved based on quantification of energy dissipation (52). It is important to note that although our extracted kinetics are in agreement with myosin-V measurements, this is not sufficient to prove that we are accessing single-molecule kinetics. Together, our results suggest that force kinetics of in vitro myosin-V is remarkably similar to the active force fluctuations in in vivo oocytes, where they drive the composite cytoplasmic-skeleton out-of-equilibrium (Table 3).

Success and limitations of this theory and experiments

Our phenomenological model is designed to capture the nonequilibrium fluctuations of vesicles in the oocyte cytoplasm. Specifically, this model is able to reproduce the deviation from equilibrium as measured by the effective energy and active force spectrum. In that respect, the agreement between model and experiments supports the underlying phenomenological picture that: 1) active fluctuations of the vesicles are mediated by the surrounding medium; 2) the complexity of the surrounding medium can be reduced to a coarse-grained representation described by local caging, 3) the damping force acting on the vesicle and the cage exhibit similar memory effects. Although this minimal approach is completely phenomenological, several studies have shown that introducing a fictitious cage coordinate has been a powerful framework for describing intermittent dynamics of a particle in a damped medium (70). And in the case of mouse oocytes, it is able to capture the nonequilibrium fluctuations of vesicles and predict force kinetics that are in agreement with single-molecule experiments on myosin-V motors. Nevertheless, this coarse-grained approach inherently neglects the microscopic details of the underlying processes.

The main drawbacks of our minimal model are: 1) We neglect any collective effects that may be occurring due to multiple motor interactions. If several motors are interacting to generate a force kick, we only capture their combined action and no information about individual motors. 2) All material properties are taken as an input to the model (as measured from experiments). Thus, the model is not able to capture how the motors may affect the material properties (e.g., cannot explain softening/stiffening (71)). Therefore it is critical that the material properties of the medium are measured in situ, and the quality of the measurements will strongly affect the model. 3) Our coarse-grained interpretation involves representing the cytoskeleton as a local cage constraining vesicle motion. Active motion of the local cage obeys Newton's second law, which typically describes the motion of a specific material point and its associated mass. In this case, because the local cage is not an actual physical object, it's mass is associated with the material that is surrounding the vesicle. This interpretation is necessary to apply Newton's second law to the active motion in our phenomenological model, and similar approaches inspired by the itinerant oscillator model have been used previously (70). Together, these drawbacks mask the underlying microscopic processes and future work will focus on gaining access to these details.

To spur future developments and improve this type of analysis we would like to point out the current limitations of the theory and experiments. In theory, our phenomenological approach to describe the cage dynamics (Eq. 2) does not track a specific material point in the cytoskeleton, making it difficult to interpret the physical basis of the memory kernel; the active process driving nonequilibrium motion is dominated by a single timescale, which may not be true in other cell types; and the number of motors driving the vesicle dynamics is not specified, because this information is typically not known in vivo. Overcoming these limitations in the theory is challenging, because tracking a

TABLE 3 Molecular-Scale Force Kinetics

	In Vivo Oocytes	Single-Molecule Myosin-V	Reference
F (pN)	0.4	0–4	(63–66)
τ (μs)	300	160–1000	(64,67,68)
Δx (nm)	20	15–25	(64,67–69)
v_{vesicle} (nm/s)	320	270–480	(65–67)

specific material point in an active material (that is constantly changing) may not be possible, and introducing multiple timescales and details about motors requires more specific information about the experimental system at hand. A useful first step could be to develop a new metric to characterize the mechanical response of active materials that does not rely on the material itself remaining invariant. In experiments, force calibration relies on the high-frequency collapse of fluctuation and response, which requires precise measurement that is often not accessible in many systems; measurements of vesicle motion are limited to a relatively small range ($\lesssim$400 nm), due to the linear range of the QPD; and rheological measurements are limited to frequencies greater than $\sim$1 Hz, due to large-scale motion in the cell. These experimental limitations could be overcome by implementing new force calibration techniques and a feedback system that continually recenters the optical trap on the vesicle.

CONCLUSIONS

We quantify the molecular-scale force kinetics of active diffusion in mouse oocytes via experiments, theory, and simulation. We find that active forces in in vivo oocytes are remarkably similar to myosin-V kinetics in vitro, and that the in vivo kinetics can be extracted from cytoplasmic fluctuations. Our results demonstrate a framework for connecting cellular scale phenomena to their underlying molecular force kinetics in vivo and provide insight on the kinetic origin of active diffusion in mouse oocytes.

SUPPORTING MATERIAL

Supporting Materials and Methods and nine figures are available at http://www.biophysj.org/biophysj/supplemental/S0006-3495(18)30212-1.

AUTHOR CONTRIBUTIONS

W.W.A. and T.B. conceived and supervised the project. W.W.A., M.B., M.A., and M.-H.V. performed experiments. É.F., N.S.G., P.V., and F.v.W. developed the theoretical model and performed simulations. W.W.A. and É.F. integrated experiment and theory. All authors contributed to data analysis and/or interpretation. W.W.A. and T.B. wrote the manuscript, which was seen and corrected by all authors.

ACKNOWLEDGMENTS

We thank Jacques Prost, Cécile Sykes, Julie Plastino, and Jean-Francois Joanny for helpful discussions. We thank Melina Schuh (MPI Göttingen) for providing the MyoVb tail plasmid, Clément Campillo for help with synthetic vesicle experiments, and Amanda Remorino for critical reading of the manuscript.

W.W.A. is a recipient of postdoctoral fellowships from La Fondation Pierre-Gilles de Gennes and Marie Curie Actions (FP7-MC-IIF-624887). M.A. is a recipient of postdoctoral fellowships from the Ligue Nationale contre le Cancer and from the Labex MemoLife. M.B. is a recipient of an AXA PhD fellowship. N.S.G. gratefully acknowledges funding from the Israel Science Foundation (580/12). M.-H.V. gratefully acknowledges the ANR (ANR-DIVACEN N°14-CE11) and the FRM Label (DEQ20150331758). T.B. was supported by the French Agence Nationale de la Recherche (ANR-11-JSV5-0002) and the Deutsche Forschungsgemeinschaft as well as by a Cells-in-Motion Cluster of Excellence grant (EXC 1003 – CiM) from the University of Münster, Germany.

REFERENCES

1. Howard, J. 2009. Mechanical signaling in networks of motor and cytoskeletal proteins. *Annu. Rev. Biophys.* 38:217–234.
2. Blanchoin, L., R. Boujemaa-Paterski, …, J. Plastino. 2014. Actin dynamics, architecture, and mechanics in cell motility. *Physiol. Rev.* 94:235–263.
3. Janmey, P. A., and C. A. McCulloch. 2007. Cell mechanics: integrating cell responses to mechanical stimuli. *Annu. Rev. Biomed. Eng.* 9:1–34.
4. Fletcher, D. A., and R. D. Mullins. 2010. Cell mechanics and the cytoskeleton. *Nature.* 463:485–492.
5. Almonacid, M., W. W. Ahmed, …, M. H. Verlhac. 2015. Active diffusion positions the nucleus in mouse oocytes. *Nat. Cell Biol.* 17:470–479.
6. Brangwynne, C. P., G. H. Koenderink, …, D. A. Weitz. 2009. Intracellular transport by active diffusion. *Trends Cell Biol.* 19:423–427.
7. Munder, M. C., D. Midtvedt, …, S. Alberti. 2016. A pH-driven transition of the cytoplasm from a fluid- to a solid-like state promotes entry into dormancy. *eLife.* 5:e09347.
8. Parry, B. R., I. V. Surovtsev, …, C. Jacobs-Wagner. 2014. The bacterial cytoplasm has glass-like properties and is fluidized by metabolic activity. *Cell.* 156:183–194.
9. Joyner, R. P., J. H. Tang, …, K. Weis. 2016. A glucose-starvation response regulates the diffusion of macromolecules. *eLife.* 5:e09376.
10. Schuh, M. 2011. An actin-dependent mechanism for long-range vesicle transport. *Nat. Cell Biol.* 13:1431–1436.
11. Holubcová, Z., G. Howard, and M. Schuh. 2013. Vesicles modulate an actin network for asymmetric spindle positioning. *Nat. Cell Biol.* 15:937–947.
12. Luksza, M., I. Queguigner, …, S. Brunet. 2013. Rebuilding MTOCs upon centriole loss during mouse oogenesis. *Dev. Biol.* 382:48–56.
13. Nikolova, V., R. Zhivkova, …, S. Delimitreva. 2012. Characterization of mouse oocytes and oocyte-cumulus complexes extracted for nuclear matrix and intermediate filaments (NM-IF). *Acta Morph. Anthropol.* 19:149–152.
14. Chaigne, A., C. Campillo, …, M. E. Terret. 2013. A soft cortex is essential for asymmetric spindle positioning in mouse oocytes. *Nat. Cell Biol.* 15:958–966.
15. Martin, P., A. J. Hudspeth, and F. Jülicher. 2001. Comparison of a hair bundle's spontaneous oscillations with its response to mechanical stimulation reveals the underlying active process. *Proc. Natl. Acad. Sci. USA.* 98:14380–14385.
16. Lau, A. W., B. D. Hoffman, …, T. C. Lubensky. 2003. Microrheology, stress fluctuations, and active behavior of living cells. *Phys. Rev. Lett.* 91:198101.
17. Mizuno, D., C. Tardin, …, F. C. Mackintosh. 2007. Nonequilibrium mechanics of active cytoskeletal networks. *Science.* 315:370–373.
18. Guo, M., A. J. Ehrlicher, …, D. A. Weitz. 2014. Probing the stochastic, motor-driven properties of the cytoplasm using force spectrum microscopy. *Cell.* 158:822–832.
19. Gallet, F., D. Arcizet, …, A. Richert. 2009. Power spectrum of out-of-equilibrium forces in living cells: amplitude and frequency dependence. *Soft Matter.* 5:2947.
20. Bursac, P., G. Lenormand, …, J. J. Fredberg. 2005. Cytoskeletal remodelling and slow dynamics in the living cell. *Nat. Mater.* 4:557–561.

21. Wilhelm, C. 2008. Out-of-equilibrium microrheology inside living cells. *Phys. Rev. Lett.* 101:028101.
22. Turlier, H., D. A. Fedosov, …, T. Betz. 2016. Equilibrium physics breakdown reveals the active nature of red blood cell flickering. *Nat. Phys.* 12:513–519.
23. Campàs, O. 2016. A toolbox to explore the mechanics of living embryonic tissues. *Semin. Cell Dev. Biol.* 55:119–130.
24. Sugimura, K., P. F. Lenne, and F. Graner. 2016. Measuring forces and stresses in situ in living tissues. *Development.* 143:186–196.
25. Azoury, J., K. W. Lee, …, M. H. Verlhac. 2008. Spindle positioning in mouse oocytes relies on a dynamic meshwork of actin filaments. *Curr. Biol.* 18:1514–1519.
26. Schuh, M., and J. Ellenberg. 2008. A new model for asymmetric spindle positioning in mouse oocytes. *Curr. Biol.* 18:1986–1992.
27. Pfender, S., V. Kuznetsov, …, M. Schuh. 2011. Spire-type actin nucleators cooperate with Formin-2 to drive asymmetric oocyte division. *Curr. Biol.* 21:955–960.
28. Dumont, J., K. Million, …, M. H. Verlhac. 2007. Formin-2 is required for spindle migration and for the late steps of cytokinesis in mouse oocytes. *Dev. Biol.* 301:254–265.
29. Verlhac, M. H., J. Z. Kubiak, …, B. Maro. 1994. Microtubule and chromatin behavior follow MAP kinase activity but not MPF activity during meiosis in mouse oocytes. *Development.* 120:1017–1025.
30. Reis, A., H. Y. Chang, …, K. T. Jones. 2006. APCcdh1 activity in mouse oocytes prevents entry into the first meiotic division. *Nat. Cell Biol.* 8:539–540.
31. Mas, J., A. C. Richardson, …, K. Berg-Sørensen. 2013. Quantitative determination of optical trapping strength and viscoelastic moduli inside living cells. *Phys. Biol.* 10:046006.
32. Blehm, B. H., T. A. Schroer, …, P. R. Selvin. 2013. In vivo optical trapping indicates kinesin's stall force is reduced by dynein during intracellular transport. *Proc. Natl. Acad. Sci. USA.* 110:3381–3386.
33. Fakhri, N., A. D. Wessel, …, C. F. Schmidt. 2014. High-resolution mapping of intracellular fluctuations using carbon nanotubes. *Science.* 344:1031–1035.
34. Gittes, F., and C. F. Schmidt. 1998. Interference model for back-focal-plane displacement detection in optical tweezers. *Opt. Lett.* 23:7–9.
35. Betz, T., and C. Sykes. 2012. Time resolved membrane fluctuation spectroscopy. *Soft Matter.* 8:5317–5326.
36. Yamada, S., D. Wirtz, and S. C. Kuo. 2000. Mechanics of living cells measured by laser tracking microrheology. *Biophys. J.* 78:1736–1747.
37. Tolić-Nørrelykke, I. M., E.-L. Munteanu, …, K. Berg-Sørensen. 2004. Anomalous diffusion in living yeast cells. *Phys. Rev. Lett.* 93:078102.
38. Jun, Y., S. K. Tripathy, …, S. P. Gross. 2014. Calibration of optical tweezers for in vivo force measurements: how do different approaches compare? *Biophys. J.* 107:1474–1484.
39. Valentine, M. T., Z. E. Perlman, …, D. A. Weitz. 2004. Colloid surface chemistry critically affects multiple particle tracking measurements of biomaterials. *Biophys. J.* 86:4004–4014.
40. Kubo, R. 1966. The fluctuation-dissipation theorem. *Rep. Prog. Phys.* 29:255–284.
41. Mizuno, D., D. A. Head, …, C. F. Schmidt. 2008. Active and passive microrheology in equilibrium and nonequilibrium systems. *Macromolecules.* 41:7194–7202.
42. MacKintosh, F. C., J. Käs, and P. A. Janmey. 1995. Elasticity of semiflexible biopolymer networks. *Phys. Rev. Lett.* 75:4425–4428.
43. Morse, D. C. 1998. Viscoelasticity of concentrated isotropic solutions of semiflexible polymers. 2. linear response. *Macromolecules.* 31:7044–7067.
44. Guo, M., A. J. Ehrlicher, …, D. A. Weitz. 2013. The role of vimentin intermediate filaments in cortical and cytoplasmic mechanics. *Biophys. J.* 105:1562–1568.
45. Ahmed, W. W., É. Fodor, and T. Betz. 2015. Active cell mechanics: measurement and theory. *Biochim. Biophys. Acta.* 1853 (11 Pt B):3083–3094.
46. Fodor, É., M. Guo, …, F. van Wijland. 2015. Activity-driven fluctuations in living cells. *EPL.* 110:48005.
47. Betz, T., M. Lenz, …, C. Sykes. 2009. ATP-dependent mechanics of red blood cells. *Proc. Natl. Acad. Sci. USA.* 106:15320–15325.
48. Ben-Isaac, E., Y. Park, …, Y. Shokef. 2011. Effective temperature of red-blood-cell membrane fluctuations. *Phys. Rev. Lett.* 106:238103.
49. Prost, J., J. F. Joanny, and J. M. Parrondo. 2009. Generalized fluctuation-dissipation theorem for steady-state systems. *Phys. Rev. Lett.* 103:090601.
50. Fodor, É., K. Kanazawa, …, F. van Wijland. 2014. Energetics of active fluctuations in living cells. *Phys. Rev. E Stat. Nonlin. Soft Matter Phys.* 90:042724.
51. Lau, A. W., and T. C. Lubensky. 2009. Fluctuating hydrodynamics and microrheology of a dilute suspension of swimming bacteria. *Phys. Rev. E Stat. Nonlin. Soft Matter Phys.* 80:011917.
52. Fodor, E., W. W. Ahmed, …, F. van Wijland. 2016. Nonequilibrium dissipation in living oocytes. *Europhys. Lett.* 116:30008.
53. MacKintosh, F. C., and A. J. Levine. 2008. Nonequilibrium mechanics and dynamics of motor-activated gels. *Phys. Rev. Lett.* 100:018104.
54. Yasuda, K., R. Okamoto, …, A. S. Mikhailov. 2017. Localization and diffusion of tracer particles in viscoelastic media with active force dipoles. *Europhys. Lett.* 117:38001.
55. Bochud, T., and D. Challet. 2007. Optimal approximations of power laws with exponentials: application to volatility models with long memory. *Quant. Finance.* 7:585–589.
56. Baczewski, A. D., and S. D. Bond. 2013. Numerical integration of the extended variable generalized Langevin equation with a positive Prony representable memory kernel. *J. Chem. Phys.* 139:044107.
57. Soares e Silva, M., B. Stuhrmann, …, G. H. Koenderink. 2014. Time-resolved microrheology of actively remodeling actomyosin networks. *New J. Phys.* 16:075010.
58. Toyota, T., D. A. Head, …, D. Mizuno. 2011. Non-Gaussian athermal fluctuations in active gels. *Soft Matter.* 7:3234.
59. Sharma, A., A. J. Licup, …, F. C. MacKintosh. 2016. Strain-controlled criticality governs the nonlinear mechanics of fibre networks. *Nat. Phys.* 12:584–587.
60. Oriola, D., R. Alert, and J. Casademunt. 2017. Fluidization and active thinning by molecular kinetics in active gels. *Phys. Rev. Lett.* 118:088002.
61. Levine, A. J., and F. C. MacKintosh. 2009. The mechanics and fluctuation spectrum of active gels. *J. Phys. Chem. B.* 113:3820–3830.
62. Robert, D., T.-H. Nguyen, …, C. Wilhelm. 2010. In vivo determination of fluctuating forces during endosome trafficking using a combination of active and passive microrheology. *PLoS One.* 5:e10046.
63. Rief, M., R. S. Rock, …, J. A. Spudich. 2000. Myosin-V stepping kinetics: a molecular model for processivity. *Proc. Natl. Acad. Sci. USA.* 97:9482–9486.
64. Cappello, G., P. Pierobon, …, J. Prost. 2007. Myosin V stepping mechanism. *Proc. Natl. Acad. Sci. USA.* 104:15328–15333.
65. Mehta, A. D., R. S. Rock, …, R. E. Cheney. 1999. Myosin-V is a processive actin-based motor. *Nature.* 400:590–593.
66. Veigel, C., S. Schmitz, …, J. R. Sellers. 2005. Load-dependent kinetics of myosin-V can explain its high processivity. *Nat. Cell Biol.* 7:861–869.
67. Uemura, S., H. Higuchi, …, S. Ishiwata. 2004. Mechanochemical coupling of two substeps in a single myosin V motor. *Nat. Struct. Mol. Biol.* 11:877–883.
68. Sellers, J. R., and C. Veigel. 2010. Direct observation of the myosin-Va power stroke and its reversal. *Nat. Struct. Mol. Biol.* 17:590–595.
69. Veigel, C., F. Wang, …, J. E. Molloy. 2002. The gated gait of the processive molecular motor, myosin V. *Nat. Cell Biol.* 4:59–65.
70. Lasanta, A., and A. Puglisi. 2015. An itinerant oscillator model with cage inertia for mesorheological granular experiments. *J. Chem. Phys.* 143:064511.
71. Ahmed, W. W., and T. Betz. 2015. Dynamic cross-links tune the solid-fluid behavior of living cells. *Proc. Natl. Acad. Sci. USA.* 112:6527–6528.

Biophysical Journal, Volume *114*

Supplemental Information

Active Mechanics Reveal Molecular-Scale Force Kinetics in Living Oocytes

Wylie W. Ahmed, Étienne Fodor, Maria Almonacid, Matthias Bussonnier, Marie-Hélène Verlhac, Nir Gov, Paolo Visco, Frédéric van Wijland, and Timo Betz

Supplementary Material for "Active mechanics reveal molecular-scale force kinetics in living oocytes "

March 12, 2018

Wylie W. Ahmed[1,2,3,†], **Étienne Fodor**[4,5], **Maria Almonacid**[6], **Matthias Bussonnier**[2,3], **Marie-Hélène Verlhac**[6], **Nir Gov**[7], **Paolo Visco**[5], **Frédéric van Wijland**[5], **Timo Betz**[2,3,8]
1 Department of Physics, California State University, Fullerton, California 92831, USA
2 Laboratoire Physico-Chimie Curie, Institut Curie, PSL Research University, CNRS UMR168, 75005, Paris, France
3 Sorbonne Universités, UPMC Univ Paris 06, 75005, Paris, France
4 DAMTP, Centre for Mathematical Sciences, University of Cambridge, Cambridge, United Kingdom
5 Laboratoire Matière et Systèmes Complexes, UMR 7057, Université Paris Diderot, 75013 Paris, France
6 CIRB, Collège de France, and CNRS-UMR7241 and INSERM-U1050, Équipe Labellisée Fondation pour la Recherce Medicale, 75005 Paris, France
5 Department of Chemical Physics, Weizmann Institute of Science, 76100 Rehovot, Israel
6 Institute of Cell Biology, Center for Molecular Biology of Inflammation, Cells-in-Motion Cluster of Excellence, Münster University, Von-Esmarch-Strasse 56, D-48149 Münster, Germany
† corresponding author (wahmed@fullerton.edu)

1 Theoretical Model

1.1 Mechanics

We consider the following equations for the vesicle dynamics in terms of the position x:

$$\int \gamma(t-t')\dot{x}(t')\mathrm{d}t' = -\kappa(x-x_0)+\xi, \quad \int \gamma(t-t')\dot{x}_0(t')\mathrm{d}t' = \kappa\zeta_\alpha v_\mathrm{A}, \tag{S1}$$

where ξ is a zero-mean Gaussian colored noise with correlations

$$\langle \xi(t)\xi(0)\rangle = k_\mathrm{B}T\gamma\left(|t|\right) \equiv C_\xi(t), \tag{S2}$$

as enforced by the fluctuation-dissipation theorem (FDT) [6], γ is the viscoelastic memory kernel, and T is the bath temperature. We assume that the process v_A has a single time scale τ that governs its decorrelation:

$$\langle v_\mathrm{A}(t)v_\mathrm{A}(0)\rangle = k_\mathrm{B}T_\mathrm{A}\mathrm{e}^{-|t|/\tau}/(\kappa\zeta_\alpha\tau) \equiv C_\mathrm{A}(t), \tag{S3}$$

where, by analogy with standard Langevin equation, we have defined an *active* temperature T_A associated to the amplitude of this process. The generalized Stokes-Einstein relation expresses the complex modulus G^* in terms of the Fourier response function $\tilde{\chi}$ as

$$G^*(\omega) \equiv 1/[6\pi R\tilde{\chi}(\omega)], \tag{S4}$$

where R is the average radius of the vesicles regarded as spherical particles. Our model is associated with the following complex modulus:

$$G^*(\omega) = \left[\kappa + \mathrm{i}\omega\tilde{\gamma}(\omega)\right]/(6\pi R), \tag{S5}$$

where $\mathrm{i}^2 = -1$. Following the choice of the memory kernel presented in the main text

$$\gamma(t) \equiv \kappa \left(\zeta_\alpha/t\right)^\alpha \Theta(t)/\Gamma(1-\alpha), \tag{S6}$$

where Γ is the Gamma function, and Θ is the Heaviside function, we deduce

$$\tilde{\gamma}(\omega) = \kappa\zeta_\alpha \left(\mathrm{i}\omega\zeta_\alpha\right)^{\alpha-1}. \tag{S7}$$

As a result, we use equation (S5) and (S7) to express G^* in terms of its real and imaginary parts, respectively denoted by G' and G'', as

$$G'(\omega) = \frac{\kappa}{6\pi R}\left[1 + (\omega\zeta_\alpha)^\alpha \cos\left(\pi\alpha/2\right)\right], \tag{S8a}$$

$$G''(\omega) = \frac{\kappa}{6\pi R}(\omega\zeta_\alpha)^\alpha \sin\left(\pi\alpha/2\right). \tag{S8b}$$

1.2 Effective energy and force spectrum

The effective energy E_{eff} is defined as

$$E_{\text{eff}}(\omega) \equiv -\omega\tilde{C}(\omega)/\left[2k_{\text{B}}\tilde{\chi}''(\omega)\right], \tag{S9}$$

where $\tilde{C}$ and $\tilde{\chi}''$ are the position power spectral density and the imaginary part of the response function in the Fourier domain, respectively. From the generalized Stokes-Einstein relation in Sec. 1.1, and by using Eq. (S8), we deduce

$$\tilde{\chi}''(\omega) = -\frac{(\omega\zeta_\alpha)^\alpha \sin\left(\pi\alpha/2\right)/\kappa}{1 + 2\left(\omega\zeta_\alpha\right)^\alpha \cos\left(\pi\alpha/2\right) + \left(\omega\zeta_\alpha\right)^{2\alpha}}. \tag{S10}$$

The Fourier transform of Eq. (S1) gives

$$\tilde{x}(\omega) = \tilde{\chi}(\omega)\left[\tilde{\xi}(\omega) + \kappa\tilde{x}_0(\omega)\right], \quad \mathrm{i}\omega\tilde{\gamma}(\omega)\tilde{x}_0(\omega) = \kappa\zeta_\alpha\tilde{v}_{\text{A}}(\omega). \tag{S11}$$

yielding the position power spectral density,

$$\tilde{C}(\omega) = |\tilde{\chi}(\omega)|^2\left[\tilde{C}_\xi(\omega) + \frac{\kappa^4\zeta_\alpha^2}{\omega^2|\tilde{\gamma}(\omega)|^2}\tilde{C}_{\text{A}}(\omega)\right], \tag{S12}$$

where ξ and v_{A} are uncorrelated noises. From Eqs. (S2) and (S3), we deduce

$$\tilde{C}_\xi(\omega) = 2k_{\text{B}}T\tilde{\gamma}'(\omega), \quad \tilde{C}_{\text{A}}(\omega) = \frac{2k_{\text{B}}T_{\text{A}}}{\kappa\zeta_\alpha\left[1 + (\omega\tau)^2\right]}, \tag{S13}$$

where $\tilde{\gamma}'$ is the real part of the Fourier memory kernel. By using (S4) and (S7-S8), $\tilde{C}$ follows as

$$\tilde{C}(\omega) = \frac{2\zeta_\alpha(\omega\zeta_\alpha)^{\alpha-1}/\kappa}{1 + 2\left(\omega\zeta_\alpha\right)^\alpha \cos\left(\pi\alpha/2\right) + \left(\omega\zeta_\alpha\right)^{2\alpha}} \times\left[\sin\left(\frac{\pi\alpha}{2}\right)k_{\text{B}}T + \frac{k_{\text{B}}T_{\text{A}}\left(\omega\zeta_\alpha\right)^{1-3\alpha}}{1 + \left(\omega\tau\right)^2}\right], \tag{S14}$$

from which we deduce the analytic expression of E_{eff} in (5) in the body of the main text. The cell force spectrum is defined as

$$S_{\text{cell}}(\omega) \equiv (6\pi R)^2|G^*(\omega)|^2\tilde{C}(\omega). \tag{S15}$$

From (S8) and (S14), one can obtain the explicit expression of this spectrum. The active part (S_{active}) and thermal part (S_{thermal}) then follow by setting $T = 0$ and $T_{\text{A}} = 0$, respectively, yielding equations (6-7) in the body of the main text. To take a closer look at the extracted kinetics we consider the average active force experienced by the vesicle, $F = \kappa v\tau$, which we can substitute directly into the definition for the active temperature (k_BT_A) and rewrite the active force spectrum in a more intuitive way as,

$$S_{\text{active}} = \underbrace{\frac{1}{(\omega\zeta_\alpha)^{2\alpha}}}_{\text{mechanics}}\ \underbrace{\frac{1}{1 + (\omega\tau)^2}\frac{2(F\zeta_\alpha)^2}{3(\tau + \tau_0)}}_{\text{motor kinetics}} \tag{S16}$$

2 Simulations

To simulate the dynamics of the vesicles, we first approximate the power law memory kernel $\gamma(t) \propto t^{-\alpha}$ as a finite sum of exponential functions (Prony series): $\gamma(t) = \sum_i c_i \mathrm{e}^{-t/\sigma_i}/\sigma_i$. Following the methods developed in [2], it is possible, with N exponential terms, to accurately approximate a power law decay over N decades. Parameters c_i and σ_i are then given by,

$$\sigma_i = \frac{10^i}{\alpha}, \quad c_i = \frac{\kappa\zeta_\alpha^\alpha}{\Gamma(1-\alpha)} \frac{10^{-i(\alpha-1)}}{\alpha \sum_j 10^{-j\alpha} \mathrm{e}^{-\alpha/10^j}} \tag{S17}$$

We approximate the power law kernel in the time window $\left[10^{N_-}, 10^{N_+-1}\right]$, where $N_- < 0 < N_+$, and $N = N_+ - N_- + 1$. Then, the index in the Prony series goes from $i = N_-$ to $i = N_+$.

With γ a sum of N exponential functions, it is possible to turn equations (1) and (2) from the main text into a $(2N+2)$-dimensional Markovian process for the variables $\left\{x, x_0, y_{N_-}, \ldots, y_{N_+}, z_{N_-}, \ldots, z_{N_+}\right\}$:

$$\sum_{i=N_-}^{N_+} \frac{c_i}{\sigma_i}(x - y_i) = -\kappa(x - x_0), \quad \sum_{i=N_-}^{N_+} \frac{c_i}{\sigma_i}(x_0 - z_i) = \kappa\zeta_\alpha v_A, \tag{S18}$$

$$c_i \frac{\mathrm{d}y_i}{\mathrm{d}t} = -\frac{c_i}{\sigma_i}(y_i - x) + \xi_i, \quad \frac{\mathrm{d}z_i}{\mathrm{d}t} = -\frac{z_i - x_0}{\sigma_i}, \tag{S19}$$

where the $\{\xi_i\}_i$ are the zero mean Gaussian noises with correlations $\langle \xi_i(t)\xi_j(t')\rangle = 2k_BTc_i\delta_{ij}\delta(t-t')$. By using Euler's methods to simulate this set of equations, the iterative equations take the following form in terms of the sampling time Δt,

$$y_i(t+\Delta t) = y_i(t) - \frac{\Delta t}{\sigma_i}\left(y_i(t) - x(t)\right) + \sqrt{\frac{2k_BT\Delta t}{c_i}}\eta, \quad z_i(t+\Delta t) = z_i(t) - \frac{\Delta t}{\sigma_i}\left(z_i(t) - x_0(t)\right) \tag{S20}$$

$$x_0(t+\Delta t) = \frac{\kappa\zeta_\alpha v_A(t+\Delta t) + \sum_i c_i z_i(t+\Delta t)/\sigma_i}{\sum_i c_i/\sigma_i}, \quad x(t+\Delta t) = \frac{\kappa x_0(t+\Delta t) + \sum_i c_i y_i(t+\Delta t)/\sigma_i}{\kappa + \sum_i c_i/\sigma_i} \tag{S21}$$

where η is random Gaussian variable with zero mean and variance equal to 1, and v_A is the stochastic process described earlier, which is computed according to the following rules:

$$v_A(t+\Delta t) = \begin{cases} v_A(t) & \text{if } v_A(t) \neq 0 \text{ with Pr. } 1 - \Delta t/\tau \\ v_A(t) & \text{if } v_A(t) = 0 \text{ with Pr. } 1 - \Delta t/\tau_0 \\ 0 & \text{if } v_A(t) \neq 0 \text{ with Pr. } \Delta t/\tau \\ U_{[-v,v]} & \text{if } v_A(t) = 0 \text{ with Pr. } \Delta t/\tau_0 \end{cases} \tag{S22}$$

where $U_{[-v,v]}$ is a uniform random number between $-v$ and v and $\tau_0 = \tau(1-p_{\mathrm{on}})/p_{\mathrm{on}}$ is the timescale over which the active burst is 0.

In order to mimic the experimental condition, we chose a sampling time $\Delta t = 10^{-4}$ s, and we aimed to simulate our process up to 10 s. Then, we have set $\{N_-, N_+\} = \{4, -2\}$, so that the power law memory kernel is well approximated in the time window$[10^{-4}, 10]$ s, with parameter values $\{\alpha, \kappa\zeta_\alpha^\alpha, N_-, N_+\} = \{0.6, 1, -4, 2\}$

Other parameters in the simulation were chosen according to the numerical fits over experimental data, and as listed in Table 1 where $p_{\mathrm{on}} = 4\%$ and $v = 60\mu\mathrm{m}\cdot\mathrm{s}^{-1}$ where $p_{\mathrm{on}} = \tau/(\tau+\tau_0)$ where $(\tau+\tau_0)$ is the total myosin-V step duration [3, 8] and v is the amplitude of the active burst velocity calculated from $v = F/(\kappa\tau)$. We also took $k_BT = 4\times10^{-21}$ J.

We started the simulation with all variables set to 0 and waited for thermalization by running the simulation for 10^3 time steps. We then start collecting position data x in order to build the histogram for the probability distribution function of the position. A total of approximately 10^5 samples were collected to arrive at the histogram in Figure 4 of the main text.

3 Laser tracking interferometry of endogenous vesicles

Laser tracking interferometry allows the displacement fluctuations of a rigid particle to be measured with high spatiotemporal resolution [4]. This technique assumes that the particle of interest is rigid. However, small endogenous particles in living cells may undergo shape fluctuations due to deformation or rotation that could affect the laser tracking signal. Therefore, we investigated the validity of using endogenous vesicles as probes for laser tracking interferometry and conclude that measured fluctuations are dominated by active displacements of the vesicle (details follow below).

We estimated the expected amplitude of vesicle deformation [1],

$$R \cdot \langle |u| \rangle = R \left[\frac{k_B T}{(\kappa(l+2)(l-1)l(l+1) + \sigma R^2 (l+2)(l-1))} \right]^{1/2} \tag{S23}$$

where u is the deformation amplitude, $k_B T$ is thermal energy, $\kappa = 50 k_B T$ is the membrane bending stiffness, $\sigma = 5 \times 10^{-5}$ N/m is the membrane tension, $R = 500$ nm is the vesicle radius, and $l = 2$ is the dominant mode of deformation. The calculated vesicle deformation (~ 4 nm) is an order of magnitude smaller than the measured fluctuations (~ 100 nm) and thus we expect that our laser-tracking of vesicles is dominated by displacements.

To test this experimentally we used several approaches. First, we confirm that the signal:noise ratio for laser interferometry (as indicated by the slope of the QPD measurement) is similar for endogenous vesicles, a colloidal bead in a cultured cell, and a colloidal bead in an index matched solution (Figure S4). Second, we perform active microrheology on a vesicle in a living oocyte at different laser powers. If vesicle deformation were significant, then the measured complex shear modulus would exhibit a systematic difference depending on laser power. Our measurements show that the moduli do not depend on laser power (Figure S5). Third, we deplete ATP in oocytes by treatment with 2mM sodium azide + 10 mM deoxyglucose to remove motion generated by active biological processes. If the signal contribution from passive vesicle deformations is comparable to displacements then we expect the amplitude of the measured fluctuations in ATP depleted cells to be comparable to the WT condition. Our measurements show that measured fluctuations in the ATP depleted case are an order of magnitude (or more) lower than in WT oocytes for all frequencies measured (Figure S6). Third, we isolated vesicles from oocytes by crushing them between two glass coverslips resulting in ruptured cells and expulsion of cytoplasmic contents into the surrounding medium. Isolated vesicles were immobilized due to adhesion to the poly-l-lysine coated coverslip. If vesicle deformation significantly influenced our laser interferometry measurement, then we expect the measured fluctuations of an immobilized isolated vesicle to be larger than an immobilized (rigid) colloidal bead. Our measurements show that measured fluctuations of an immobilized vesicle are comparable to an immobilized bead (Figure S7) (high-frequency deviation results from shot noise due to a lower refractive index of the vesicle relative to the bead). Fourth, we measured the response of immobilized vesicles by applying force with high laser power (120 mW). This quantifies the response due to only vesicle deformation (since it is immobilized). Our measurements show that deformation of an immobilized isolated vesicle (red data points) is more than an order of magnitude smaller than the response measured with vesicles in WT oocytes (blue data points) (Figure S8). Therefore, in living cells, our measurements are dominated by vesicle displacements and not deformations. Lastly, we created synthetic vesicles via electroformation as done previously [1] to allow direct measurement in a well-controlled environment. Vesicles were placed in a hypertonic environment (175 mOsm/kg sucrose inner buffer and 185 mOsm/kg NaCl outer buffer) to promote membrane fluctuations. The power spectral density of synthetic vesicles (~ 1 μm) is fit well by the theory for rigid beads (Figure S9 (left)) but is not fit well by the theory for deformable vesicles as seen at intermediate frequencies (Figure S9 (right)). Note that the extracted fitting parameters for the rigid bead theory agree with expected values, but to obtain a fit for the vesicle theory the fitting parameters must take on unrealistic values for our experimental conditions. Together, these experiments suggest that small vesicles behave indistinguishably from rigid particles in our experiments and serve as suitable probes for laser tracking interferometry.

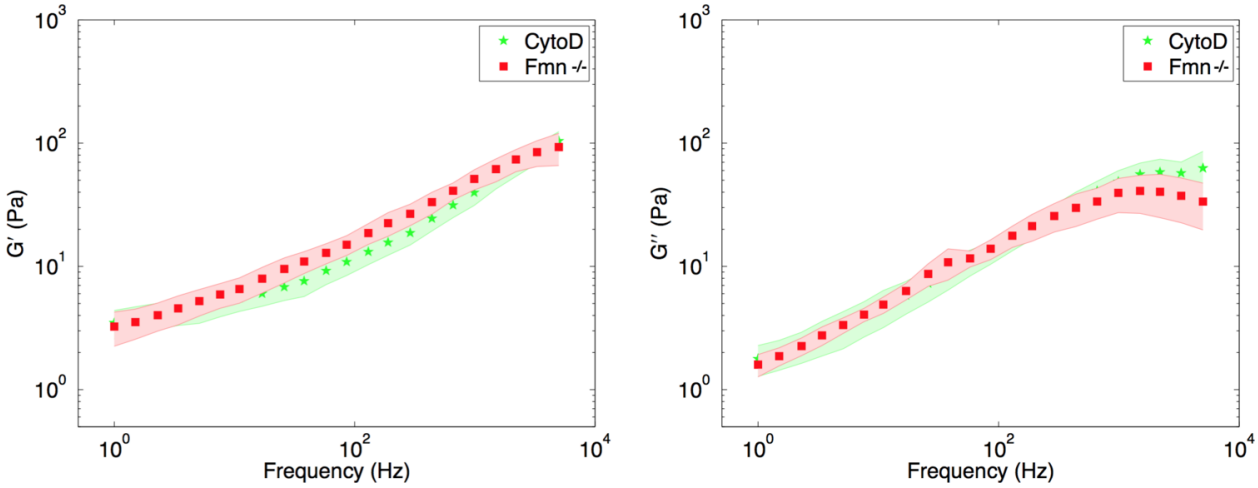

Figure S1: Viscoelastic shear moduli of Fmn -/- oocytes are not significantly different from WT + Cytochalasin-D oocytes. To confirm that actin filaments do not provide significant mechanical resistance, we treated WT oocytes with cytochalasin-D (1 μg/ml) for 2 hours. Subsequent AMR measurements showed their mechanical properties were not different than Fmn -/- oocytes. ($n_{\mathrm{Fmn}-/-} = 23$ and $n_{\mathrm{cytoD}} = 16$; shaded region indicates standard error of the mean)

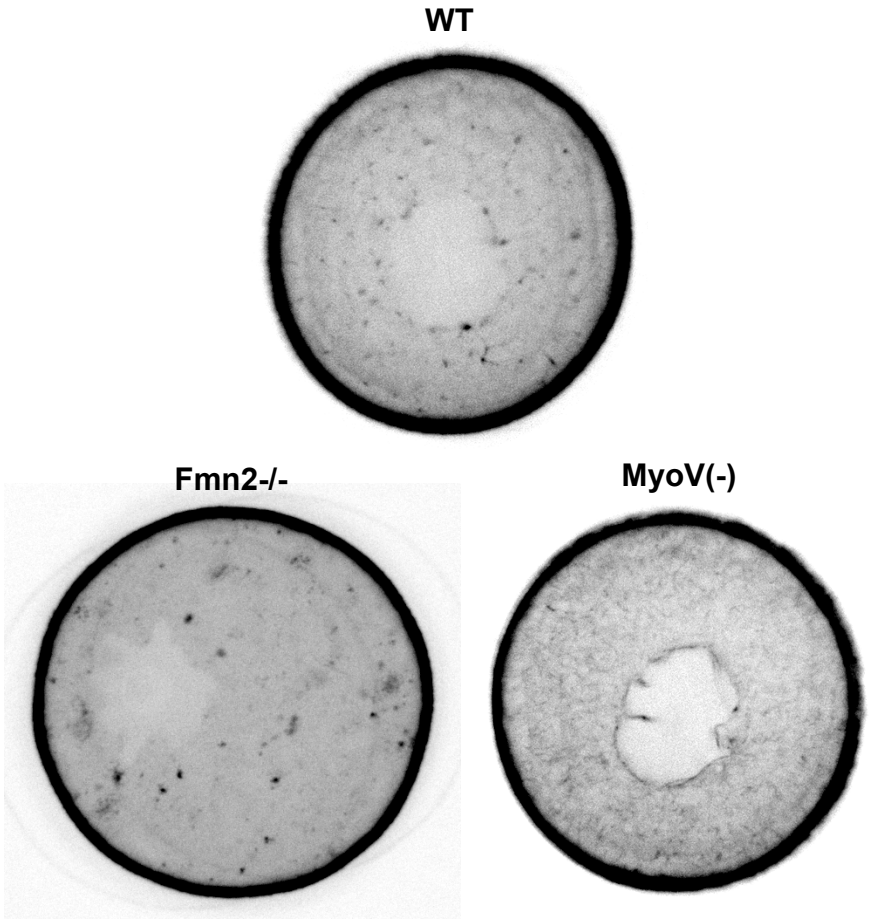

Figure S2: The actin meshwork was visualized with GFP-UtrCH to show the actin meshwork. WT oocytes exhibit a network of actin positive vesicles connected by actin filaments to create a meshwork. Fmn2 -/- exhibited punctate actin but no visible meshwork. MyoV(-) exhibit an increased density actin meshwork relative to WT. Images were captured at 37 degrees Celsius using a 40x objective (1.25NA) on a Leica DMI6000B microscope enclosed in a thermostatic chamber (Life Imaging Service) equipped with a CoolSnap HQ2/CCD-camera (Princeton Instruments) coupled to a Sutter filter wheel (Roper Scientific) and a Yokogawa CSU-X1-M1 spinning disc. (oocyte diameter is 80 μm)

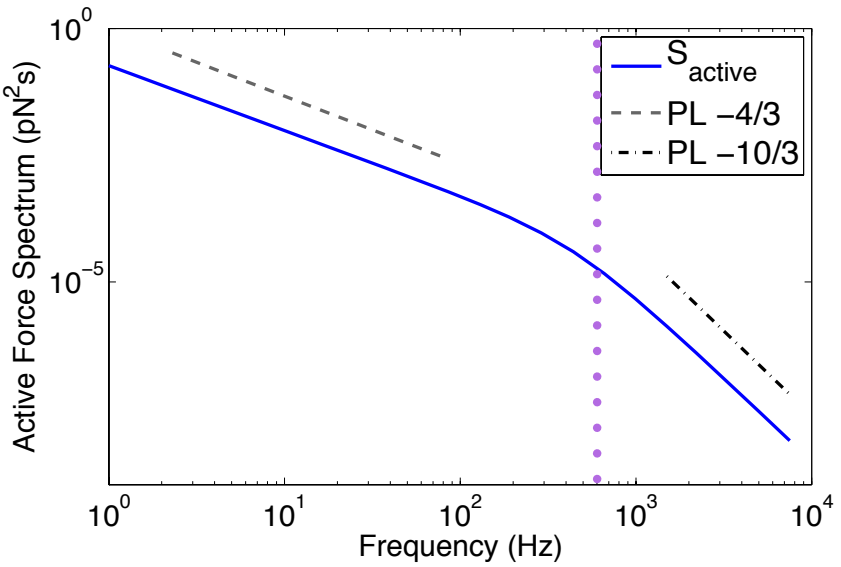

Figure S3: The active force spectrum shows two distinct power-law (PL) behaviors at low ($f^{-2\alpha}$) and high frequency ($f^{-2\alpha-2}$) compatible with the experimentally measured $\alpha \sim 2/3$.

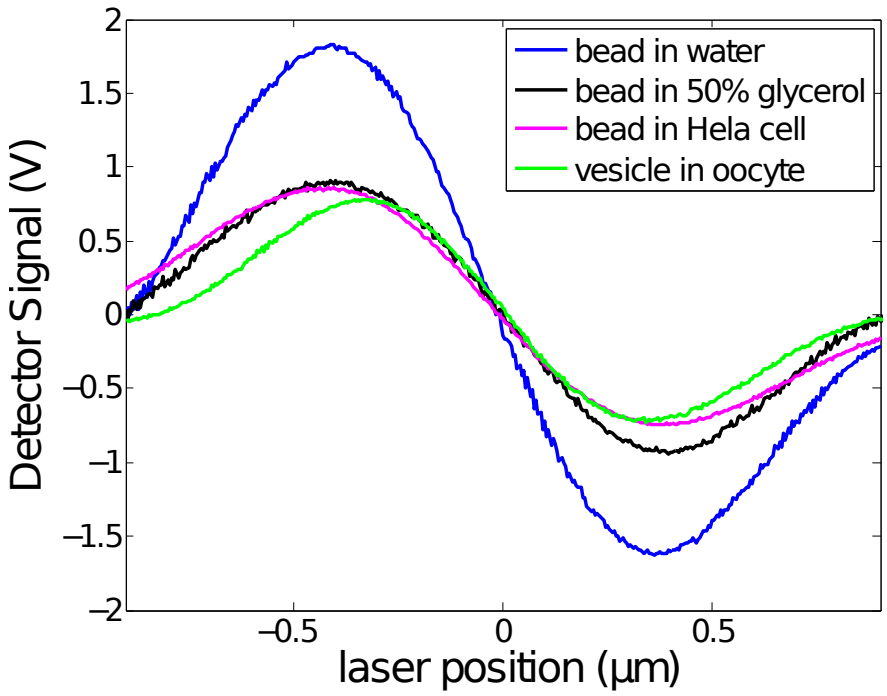

Figure S4: QPD voltage vs. laser position for various conditions. The slope of the central linear region is indistinguishable between a vesicle (diameter of approximately 1 micron) in an oocyte (green), a 1 micron colloidal bead in a Hela cell (magenta), and a 1 micron colloidal bead in an index matched solution of 50:50 water:glycerol. For comparison, the slope of a 1 micron colloidal bead in pure water is significantly steeper due to the higher difference in index of refraction. This measurement shows that the signal:noise ratio for the QPD measurements is similar for endogenous vesicles and colloidal beads in cells and index matched media.

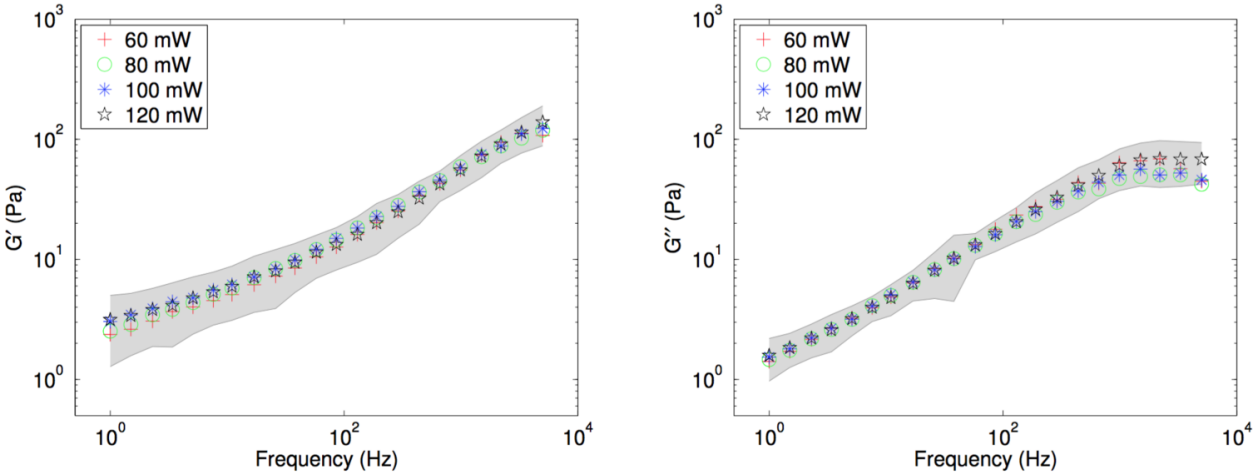

(a) elastic moduli (b) viscous moduli

Figure S5: Viscoelastic shear moduli of oocytes is not affected by the laser power used for active microrheology. Measurements were performed on the same vesicle at different laser powers and a representative example is shown. ($n = 23$; shaded region indicates standard deviation of all measurements)

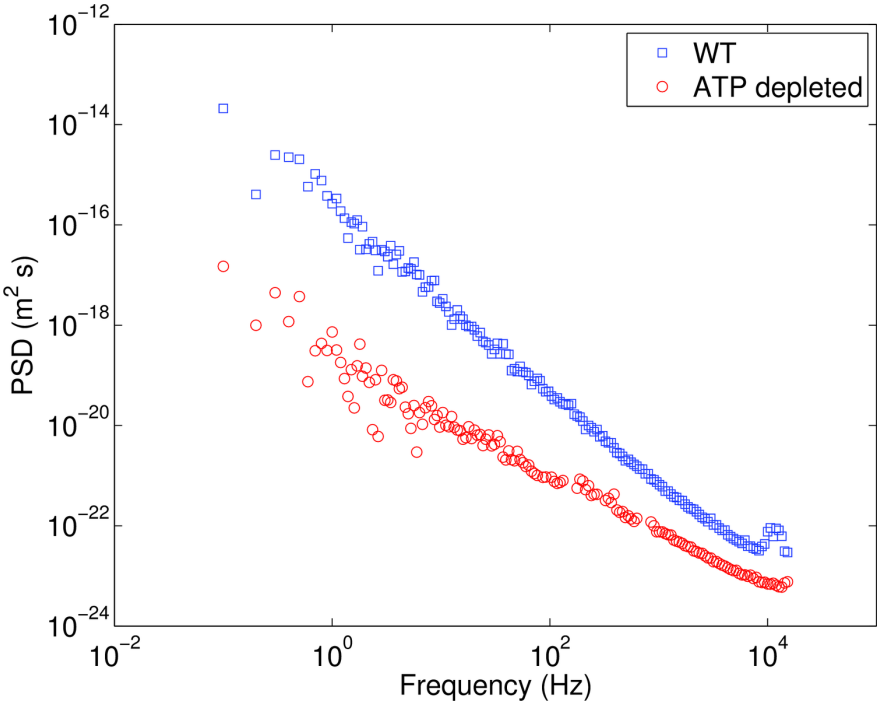

Figure S6: Power spectral density of measured fluctuations in ATP depleted oocytes are significantly lower than in WT oocytes. (local peaks from resonant frequencies of piezo stage feedback have been removed from data)

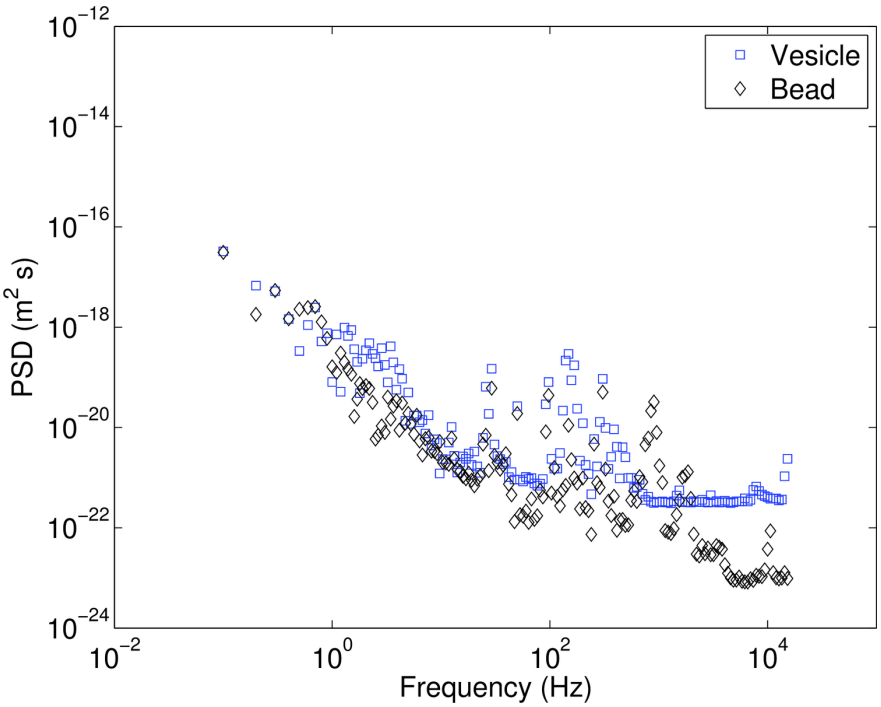

Figure S7: Power spectral density of measured fluctuations in an isolated oocyte vesicle are not significantly different than a colloidal bead (both of ∼1 micron diameter).

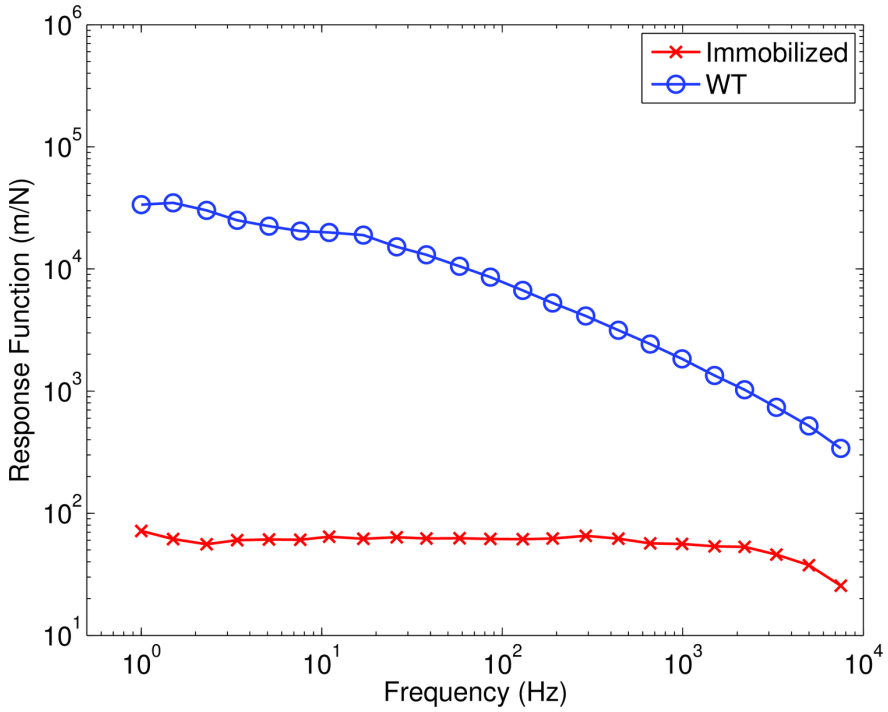

Figure S8: The force response of an isolated and immobilized vesicle is at least an order of magnitude smaller than for freely moving vesicles in WT oocytes. The forced response was measured on a ~ 1 micron diameter vesicle at 120 mW laser power. This measurement suggests that deformations of the vesicle itself are a small contribution to our measured signal. ($n_{immobilized} = 8$, $n_{WT} = 8$)

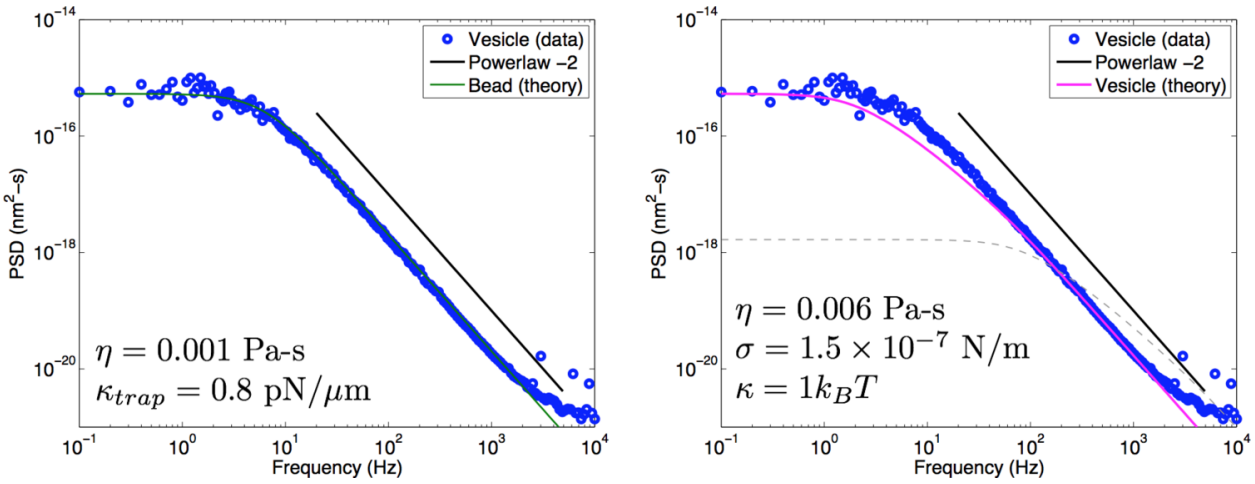

Figure S9: The power spectral density (PSD) of a trapped synthetic vesicle ($\sim$ 1 micron at 5 mW laser power) made by electroformation [1] is compared with the theory for a rigid bead (left) and a deformable vesicle (right). (Left) The measured data for a vesicle is fit well by the theory for a rigid bead trapped in a harmonic potential [5] and the extracted fit parameters ($\eta = 0.001$ Pa-s, $\kappa_{trap} = 0.8$ pN/μm) agree with the viscosity of water and the optical trap stiffness. (Right) The measured data is not fit well by the theory for a deformable vesicle [7], showing deviation at intermediate frequencies and unrealistic fit parameters. Note that for the vesicle theory the extracted viscosity ($\eta = 0.006$ Pa-s) is six times higher than expected for water and the membrane tension ($\sigma = 1.5 \times 10^{-7}$ N/m) and membrane bending stiffness ($\kappa = 1k_BT$) are an order of magnitude lower than expected for these vesicles [1]. The PSD expected for a vesicle with realistic physical parameters ($\eta = 0.001$ Pa-s, $\sigma = 1 \times 10^{-6}$ N/m, and $\kappa = 10k_BT$) is shown as a dotted-gray line [1]. This measurement suggests that small vesicles are best approximated by the rigid bead theory (left) and are suitable for laser-tracking interferometry. ($n = 16$)

References

[1] Timo Betz and Cécile Sykes. Time resolved membrane fluctuation spectroscopy. *Soft Matter*, 8(19):5317–5326, 2012.

[2] Thierry Bochud and Damien Challet. Optimal approximations of power laws with exponentials: application to volatility models with long memory. *Quantitative Finance*, 7(6):585–589, dec 2007.

[3] G Cappello, P Pierobon, C Symonds, L Busoni, JC Gebhardt, M Rief, and J Prost. Myosin V stepping mechanism. *Proc Natl Acad Sci U S A*, 104:15328–33, Sep 2007.

[4] F Gittes and CF Schmidt. Interference model for back-focal-plane displacement detection in optical tweezers. *Opt Lett*, 23:7–9, Jan 1998.

[5] Frederick Gittes and C. F. Schmidt. Thermal noise limitations on micromechanical experiments. *European Biophysics Journal*, 27(1):75–81, jan 1998.

[6] R Kubo. The fluctuation-dissipation theorem. *Rep. Prog. Phys.*, 29(1):255–284, jan 1966.

[7] Scott T. Milner and S. A. Safran. Dynamical fluctuations of droplet microemulsions and vesicles. *Phys. Rev. A*, 36(9):4371–4379, nov 1987.

[8] Sotaro Uemura, Hideo Higuchi, Adrian O Olivares, Enrique M De La Cruz, and Shin'ichi Ishiwata. Mechanochemical coupling of two substeps in a single myosin V motor. *Nat Struct Mol Biol*, 11(9):877–883, aug 2004.